

ATLAS

ATLID Algorithms and Level 2 System Aspects

Algorithm Theoretical Basis Document (ATBD) for High-Resolution Lidar Extinction Backscatter and Depolarization ratio (A-EBD ATBD)

Code : EC-TN-KNMI-ATL-021
Issue : 1.3
Date : 09/06/2011
Authors : D.P. Donovan
G-J van Zadelhoff
S. Berthier

Associated Products: A-EBD and A-TC

This page intentionally left blank

Change Log

Issue	Revision	Date	Reason for Change	Author
1	0	05/04/2011	First Complete Draft	D.P. Donovan
1	1	25/04/2011	Post IR edits	D.P. Donovan
1	2	26/05/2011	Post FM edits	D.P. Donovan, GJvZ
1	3	09/06/2011	Post PA Edits (Annex has changed and `striped` figures fixed)	D.P. Donovan

Table of Contents

1	Purpose and Scope	10
2	Applicable and Reference Documents	11
2.1	Applicable documents	11
2.2	Reference & Related documents	11
2.3	Scientific References	12
3	Scientific Background of the algorithm	13
3.1	Algorithm history	13
3.2	Algorithm introduction	13
3.3	Physical/mathematical Background	13
3.3.1	Use of the Rayleigh Channel	16
3.3.2	Multiple Scattering	17
3.3.2.1	Analytical model of Hogan	17
3.3.2.2	Platt's approach	19
3.3.3	Construction of Total Signal and Cross-Talk effects	22
3.3.4	Horizontal Signal binning	23
3.3.5	Optimal Estimation procedure	24
3.3.6	Determination of inversion layers and Specification of a priori values	27
3.3.7	Optimization procedure	28
3.3.8	Error Estimates	30
4	Justification for the selection of the algorithm	31
5	Mathematical algorithm Description	32
5.1	Input parameters	32
5.2	Input Configuration parameters	35
5.3	Output parameters	41
5.3.1	A-ECB outputs	41
5.3.2	A-TC associated outputs	44
5.4	Algorithm flow charts and Definition	46
5.4.1	Overall Algorithm Structure	46
5.4.2	Expanded View of A1: Find Layering, Grouping and Classification	47
5.4.3	Expanded view of A4: Mimimize Optimal Estimation Cost function	49
5.4.4	Expanded view of Box C10: Cost function routine	50
5.4.5	Expanded view of Box D5: Call Klett_General_Grad	51
5.4.6	Expanded View of Box A7: Calculate Output Products and Errors	52
5.5	Algorithm Definition	53
5.5.1	A1: Find Layering, Grouping and Classification	53
5.5.1.1	B1: Select sub-columns:	53
5.5.1.2	B2: Apply threshold to Feature Mask data	54
5.5.1.3	B3: Find sub-groups, average signals (see also Section 3.3.4 Horizontal Signal binning)	54
5.5.1.4	B4: Find Layers	55
5.5.1.5	B5: Find Sub-Layers using R and Depol	55
5.5.1.6	B6: Find layer average R and δ	56
5.5.1.7	B7: Classification of Layers	56
5.5.1.8	B8: Form classification mask	57

5.5.1.9	B9: Find Layers using Depol, S, and R	57
5.5.1.10	B10: Calculate layer average S and σ_s values.	57
5.5.1.11	B11: Classification of aerosol layers	57
5.5.1.12	B12: Form aerosol type mask.	57
5.5.1.13	B13: Merge large-scale derived and 1-km scale Masks.	57
5.5.1.14	B14: Update layer structure	57
5.5.2	A2: Calculate Average Non-crosstalk Corrected Signals and Uncertainties for each Group	58
5.5.3	A3: Initialize State Vector	58
5.5.4	A4: Minimize Optimal Estimation Cost function.....	58
5.5.4.1	C1: Set calc_errors=false, Eta_invert=true.....	58
5.5.4.2	C2: Call BGFS solver	58
5.5.4.3	C3: Set calc_error=false etc.....	58
5.5.4.4	C4: Set $M_{OLD}(z) = M_t$ and $M_t(z) = M(z)$	58
5.5.4.5	C5: Call BGFS solver	58
5.5.4.6	C6: Set not_converged=false and MS_loops++	59
5.5.4.7	C7: MS_loops gt. Max_MS_loops	59
5.5.4.8	C8: If ((Target_type(ig,iz) etc.....	59
5.5.4.9	C9: Done	59
5.5.4.10	C10: Cost function routine.....	59
5.5.5	A5: Update Classification.....	61
5.5.6	A6: Has Classification Changed ?	62
5.5.7	A7: Calculate Output Products and Errors.....	62
5.5.7.1	F1: Set calc_errors=true. Eta_invert=false	62
5.5.7.2	F2: Call Cost function.....	62
5.5.7.3	F3: Calculate β and $\frac{\partial\beta}{\partial B}$	62
5.5.7.4	F4: Set calc_errors=false.	62
5.5.7.5	F5: Calculate Curvature Matrix etc.....	62
5.5.7.6	F6: Calculate covariance Matrices.....	63
5.5.7.7	F7: Calculate Layer integrated quantities and errors	64
6	Algorithm performance, sensitivity studies, limitations	65
6.1	Simple 1-D Cirrus Cases: a priori S sensitivity	65
6.2	Simple 1-D Cirrus Cases: a priori Cross-Talk coefficients sensitivity	69
6.3	2D Examples: The ECSIM “Standard-Scene”	71
6.4	2D Examples: ECSIM “Fractal Cirrus Scene”	76
6.5	SAMUM1Desert Dust Aerosol scene.....	80
6.5.1	Sensitivity to Calibration Errors	85
7	Validation Status.....	87
8	Annex A: Technical implementation	88
8.1	External models	88

List of Tables

Table 1: Required input parameters.....	35
Table 2: Algorithm input configuration parameters.	41
Table 3: A-EBD Related output parameters	41
Table 4: A-TC associated outputs.....	44
Table 5: Cirrus cases characteristics	65
Table 6: Extinction-to-backscatter ratios and effective area weighed radii retrieved for the different cases along with their error estimates. Values of $S = 20.8$ 1/sr $R_a = 42.7$ microns were used in the forward model simulations.	66
Table 7: C_x sensitivity cases.	69
Table 8: Results for Cases 3a and 3b.....	69
Table 9: True values compared to the a priori values used in standard-scene inversion shown here. Cirrus-1 refers to the thinner upper-level cirrus cloud region while Cirrus-2 refers to the lower level extension.....	71

List of Figures

Figure 1: Schematic relationship of the algorithm described in this ATBD (red-box) with respect to other lidar-only (L2a) algorithms as well as relevant MSI and CPR synergetic (L2b) algorithms.	10
Figure 2: High level simplified schematic of the core approach of the algorithm Note that within this diagram multiple-scattering is not explicitly treated.	16
Figure 3. Sample comparison between the ECSIM lidar Monte-Carlo multiple scattering model and the analytical model due to Hogan (2006). (Left) Mie co-polar and (Right) Rayleigh channel co-polar returns for an ice cloud of OT 0. and an effective radius of 30.7 microns. Black solid: ECSIM results. Dashed Black: Single scattering results. Solid Grey: Hogan's model results for the true value of Ra. Dashed Grey from left to right: Hogan's model results for Ra=10, 25.0, 50, 100 and 200 microns respectively.	18
Figure 4: As Figure 3, however the results for Hogan's model are shown only for Ra=25.0 microns and the Red lines shown the result of predicting M using Eq. (3.15) with $\eta=0.55$	20
Figure 5: High level schematic describing how Multiple Scattering is accounted for in this algorithm.	21
Figure 6: Schematic depiction of the horizontal averaging strategy employed within this algorithm.	24
Figure 7: Normalized probability as a function between the ratio of a variables value to its expected value for (solid-line) Eqn. (3.30), (dotted-line) $\ln(x^f)$ is assumed to be Gaussian (dash-dotted) case where x^f is Gaussian. Note that for x-axis values greater than one that the solid and dash-dotted lines overlap. For all lines it has been assumed that $\sigma_{x^f}^2 = 1$	27
Figure 8: Left: Simplified Cost function as a function of normalized values of $\alpha(z_m)$ and S . Right: sample cross section through the data shown in the Left panel. Conditions correspond to a single layer cloud with an optical depth of 1.5. No multiple-scattering effects were considered.	29
Figure 9: Left: Simplified Cost function with the penalty term added shown as a function of normalized values of $\alpha(z_m)$ and S . Right: sample cross section through the data shown in the Left panel. Conditions correspond to a single layer cloud with an optical depth of 1.5. No multiple-scattering effects were considered.	30
Figure 10: High-level structure of the main algorithm. Here the Yellow trapezoids represent input or output data sets.	46
Figure 11: Schematic description of the steps involved in the layer, grouping and classification step (A1: Figure 10). Here the light-Grey-Blue boxes denote processes that are separately described in detail in [A-TC-ATBD].	47
Figure 12. Expanded schematic of box B3 of Figure 11.	48
Figure 13: Expanded view of Box A4: Minimize Optimal estimation cost-function in Figure 10.	49
Figure 14. Expanded view of Box C10: Cost function routine in Figure 13.	50
Figure 15. Expanded view of Box D5: Call Klett_General_Grad in Figure 14.	51
Figure 16: view of Box A7: Calculate Output Products and Errors in Figure 10.	52

Figure 17: Inversion results for Case 1a (Top), 1b, (Middle) and 1c (Bottom). In the 3rd column the Red lines show the first guess extinction retrieval and the Black-line the best estimate profile. In the 2nd column the Red lines shows the first-guess predicted Rayleigh signal while the Blue-line shows the best estimate profile. The 4th column shows the cloud optical depth. 67

Figure 18: Inversion results for Case 2a (Top), 2b, (Middle) and 2c (Bottom). In the 3rd column the Red lines show the first guess extinction retrieval and the Black-line the best estimate profile. In the 2nd column the Red lines shows the first-guess predicted Rayleigh signal while the Blue-line shows the best estimate profile. The 4th column shows the cloud optical depth. 68

Figure 19: (Top) Same as top of Figure 18 (Middle) same as Case 1a except with at 50% underestimation of C_x (Bottom) 50% overestimation. In the Middle and Bottom panels the light-Blue line shows the First-Guess profile of the Rayleigh Signal. 70

Figure 20: Extinction and S for the “Standard” ECSIM scene. 72

Figure 21: (Top) Cross-talk corrected Mie channel signals corresponding to night-time corresponding to Figure 20 (Middle) Rayleigh channel signals and (Bottom) the corresponding FeatureMask used derived from the Mie channel signals and used as input in this algorithm. 73

Figure 22: Top : “True” Extinction. Middle: Retrieved best estimate and (Bottom) Estimated error. The blanked regions show areas where clouds or aerosols may be presented but no retrieval is possible due to too low SNR. 74

Figure 23: Top: Ideal Extinction-to-Backscatter ratio. Middle retrieval and (Bottom) estimated error. 75

Figure 24: 3D view of the extinction field for the fractal-cirrus scene. 76

Figure 25: Ideal extinction (Top Left), Mie channel signals (Top right), Rayleigh channel signals (Bottom-Left) and FeatureMask (Bottom-Right) corresponding to the crosssection in Figure 24. 77

Figure 26: Top-Left : “True” Extinction. Top-Right: Retrieved best estimate. Bottom-Right Estimated error and Bottom-Left: Extinction retrieval produced by the first-guess state-vector. 78

Figure 27: Top: Ideal Extinction-to-Backscatter ratio. Middle retrieval and (Bottom) estimated error. 79

Figure 28: Extinction field and 10km horizontally averaged Mie and Rayleigh signals. The large extinction values below 2 km correspond to the surface. 81

Figure 29: Results of the inversion algorithm applied to 1-km data. Top-Left: Extinction. Bottom-Left: Estimated extinction error. Top-Right: Extinction-to-Backscatter estimated error. Bottom-Right: Estimated error in S 82

Figure 30: Sample 1km inversion result profiles corresponding to the first retrieval column of Figure 29. 82

Figure 31: 50km horizontal averages of 1-km inversion results. The Black-lines show the retrieval results while the Red-lines show the true average profile. Left-Column: $S_a = 70$ sr. Middle-Column: $S_a = 35$ sr. Right-Column $S_a = 140$ sr. Top-Row: Average Optimal-Estimate profile. Bottom-Row: Average First-guess profile. 83

Figure 32: Inversion results applied to 25km averaged signals. The Black-lines show the retrieval results while the Red-lines show the true average profile. Left-Column: $S_a = 70$ sr. Middle-Column: $S_a = 35$ sr. Right-Column $S_a = 140$ sr. Top-Row: Average Optimal-Estimate profile. Bottom-Row: Average First-guess profile. 84

Figure 33: Inversions applied to 25 km averaged signals. (Top) perfect calibration assumed (Middle) calibration coefficients 20% too high (Bottom) calibration coefficients 20% too-low. The Blue line in the middle panes shows the starting value of the Rayleigh backscatter profile while the Red-lines shows the first-guess extinction retrieval.86

1 Purpose and Scope

This document describes the Lidar only Extinction, Backscatter and Depolarization L2a algorithm developed within the ATLAS project. This algorithm outputs high horizontal (approx 1-km) and vertical (approx 100 m) resolution profiles of lidar extinction, backscatter, optical depth and particle type. The relationship between this algorithm and other algorithms developed within ATLAS is shown in Figure 1. This document presents theoretical background of the algorithm (Section 3) as well as describing practical implementation aspects such as inputs (Section 5.1), outputs (Section 5.3) and algorithm structure (Section 5.3.2). Examples applications of the algorithm are given in Section 6 and an overview of the status of the algorithm is given in Section 7.

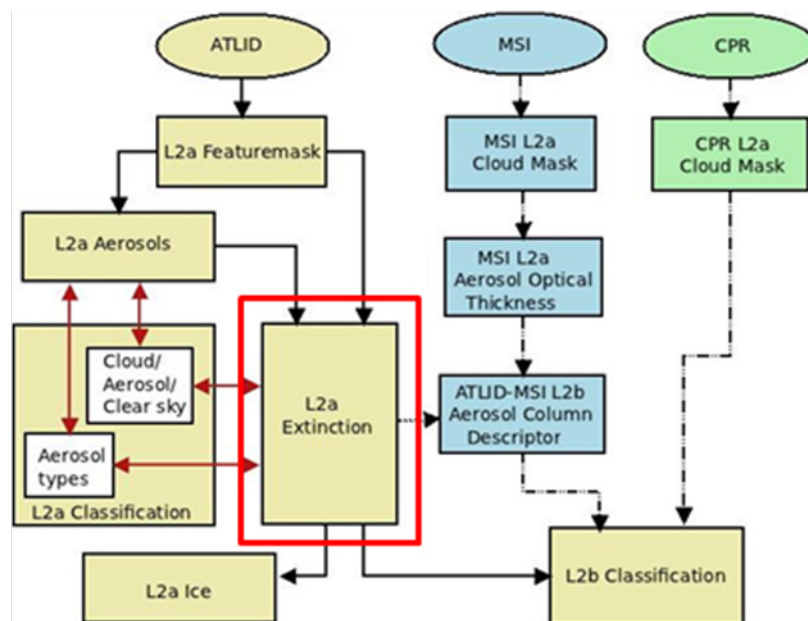


Figure 1: Schematic relationship of the algorithm described in this ATBD (red-box) with respect to other lidar-only (L2a) algorithms as well as relevant MSI and CPR synergetic (L2b) algorithms.

2 Applicable and Reference Documents

2.1 Applicable documents

<i>Reference</i>	<i>Code</i>	<i>Title</i>	<i>Issue</i>	<i>Date</i>
MRD	EC-RS-ESA-SY-012	EarthCARE Mission Requirements Document	5	2/11/2006

2.2 Reference & Related documents

<i>Reference</i>	<i>Code</i>	<i>Title</i>	<i>Issue</i>	<i>Date</i>
CASPER-FINAL	CASPER-DMS-FR-01	CASPER Final Report	1.1	30/01/2009
A-FM-ATBD	EC-TN-KNMI-ATBD-A-FM-010	ATLAS Featuremask ATBD	2.2	26/05/2011
A-FM-PDD	EC-TN-KNMI-PDD-A-FM-011	ATLAS Featuremask PDD	1.0	26/05/2011
ATLAS-PARD	EC-TN-KNMI-ATL-005	ATLAS Products and Algorithms Requirements Document (PARD)	1.1	10/03/2010
EarthCARE	EC-ICD-ESA-SYS-0314	EarthCARE product Table	1.3	15/06/2010
A-TC-ATBD	EC-TN-KNMI-ATL-ATBD-A-TC-022	ATLID L2a Classification ATBD	2.0	25/04/2011
A-AER-ATBD	EC-TN-KNMI-ATL-ATBD-A-AER-019	ATLID L2a Aerosol Extinction, Backscatter and Depolarization	1.1	25/04/2011
ICAROHS-TN2	ICAROHS-TN2	ICAROHS ESA project Technical note describing scene creation.	1.0	14/03/2011
EADS-A-L1-ATBD	ATLID ECGP ATBD (D-AT20)	ATLID Level 1 processor ECGP	3.0	15/09/2011

2.3 Scientific References

Keyword	Reference
Hogan 2006	Fast, approximate calculation of multiply scattered lidar returns, <i>Applied Optics</i> , 45, 5984-5992 (2006).
Hogan and Kew 2005	Hogan, R. J., and S. F. Kew: A 3D stochastic cloud model for investigating the radiative properties of inhomogeneous cirrus clouds. <i>Q. J. R. Meteorol. Soc.</i> , 131, 2585-2608 (2005)
Klett 1985	Klett, J.D. Lidar inversion with variable backscatter/extinction ratios <i>Applied Optics</i> , Vol. 24, Issue 11, pp. 1638-1643 (1985) doi:10.1364/AO.24.001638
Platt 1973	Platt, C. M. R., 1973: Lidar and radiometric observations of cirrus clouds, <i>J. Atmos. Sci.</i> , 30, 1191–1204.
Press et al. 1992	Press, W.H., Teukolsky, S.A., Vetterling, W.T. and Flannerty, B.P. (1992), <i>Numerical Recipes in C: The Art of Scientific Computing</i> , (2nd Edition), Cambridge University Press, New York.
Shiple 1983	Shiple, S.T., D.H. Tracy, E.W. Eloranta, J.T. Trauger, J.T. Sroga, F.L. Roesler and J.A. Weinman, "A High Spectral Resolution Lidar to Measure Optical Scattering Properties of Atmospheric Aerosols, Part I: Instrumentation and Theory", <i>Applied Optics</i> , 23, 3716-3724, 1983
Rodgers 2000	Rodgers, C.D., "Inverse methods for Atmospheric Sounding; Theory and Practice", Series on Atmospheric, Oceanic and Planetary Physics-Vol. 2, World Scientific, ISBN 981-02-2740-X, 2000.

3 Scientific Background of the algorithm

3.1 Algorithm history

This algorithm is built upon the combined Rayleigh-Mie lidar extinction and backscatter retrieval algorithm developed within the CASPER project (see [CASPER-FINAL]). However, several shortcomings with respect to the CASPER developments were identified, this led to a significant amount of new development, which, ultimately led to the creation of an almost wholly new algorithm.

3.2 Algorithm introduction

The Rayleigh signal from a HSRL lidar can be used to estimate the extinction profile in a rather direct manner [Shipley, 1983] by estimating the derivative of the range-corrected logarithmic signal. However, the applicability of this method is limited due to a high required SNR ratio. Thus, one can assert that accurate but low-precision extinction information is, in general, provided by the Rayleigh signal. In contrast, extinction information can also be extracted from the Mie signal channel which, in general, may be viewed as less accurate (since factors such as the extinction-to-backscatter ratio must be specified in order to “invert” the signal [Klett 1985]) but more precise (since the SNR ratio of the input data does not impact the derived extinction product to the same degree of extent.).

Taking into account these two observations, it is advantageous to formulate a retrieval procedure which simultaneously uses both the Rayleigh and Mie signals in order to combine the accurate but less precise Rayleigh channel derived information with the less-accurate but more precise information derived using the Mie channel. The essence of the algorithm described in this ATBD, is to perform a Klett-like retrieval using an S profiles which yields an extinction profile which, in turn, enables an optimal reconstruction of the observed Rayleigh channel signal. It is thought that an optimal-estimation based variational approach is best suited for this purpose.

In contrast to the earlier algorithm developed during the CASPER project, the approach developed here is (to a degree) tolerant of cross-talk correction errors. In particular, the procedure in essence performs its own cross-talk correction procedure and estimates of the actually cross-talk correction coefficients are generated.

3.3 Physical/mathematical Background

In this section, we give an overview of the general background theory and major techniques that the algorithm relies on. In Section 4, more detailed specific information is given.

The algorithm makes use of the total backscatter signal as well as the Rayleigh signal profile. It should be noted that the total signal is not directly measured by ATLID.

However, the total signal can be reconstructed by appropriately combining the separate Mie co-polar, Rayleigh co-polar and Total cross-polar channels. This issue is addressed in detail later.

The total (calibrated) backscatter signal measured by a lidar can be written as

$$p_t(z) = \frac{(\beta_M(z) + \beta_R(z))}{r(z)^2} \frac{1}{M(z)} \exp\left[-2 \int_{z_{lid}}^z (\alpha_M(z') + \alpha_R(z')) dr'\right] \quad (3.1)$$

where z is altitude (above MSL), $r(z)$ is the range from the lidar, z_{lid} is the lidar altitude, β denotes backscatter, α denotes extinction, and the subscripts M and R are used to distinguish between Mie (aerosol+cloud) and Rayleigh scattering extinction and backscatter respectively. M is a multiple scattering correction factor that must be calculated with the aid of a model.

The Rayleigh related terms in Eq.(3.1) are simply related to the atmospheric density profile which is assumed to be known. However, the presence of two unknowns ($\alpha_M(z)$ and $\beta_M(z)$) and only one measured quantity ($p_t(z)$) means that Eq.(3.1) cannot be directly solved (inverted).

Without loss of generality, we can write:

$$\alpha_M(z) = S(z)\beta_M(z) \quad (3.2)$$

where $S(z)$ is the so-called extinction-to-backscatter ratio and depends on the characteristics of the scatterers being probed. Eq.(3.1) can then be re-written as

$$\begin{aligned} b_t(z) &\equiv p_t(z)r(z)^2 M(z) \exp\left[2 \int_{z_{lid}}^z \alpha_R(z') dr'\right] \\ &= \frac{1}{S(z)} (\alpha_M + S(z)\beta_R(z)) \exp\left[-2 \int_{z_{lid}}^z \alpha_M(z') dr'\right] \end{aligned} \quad (3.3)$$

where we have, in effect, corrected the signal for the range dependence, Rayleigh extinction and multiple scattering. We further note that if we define

$$B_t(z) = \exp\left[-2 \int_{z_{lid}}^z S(z')\beta_R(z') dr'\right] b_t(z)S(z). \quad (3.4)$$

Then

$$B_t(z) = \alpha'(z) \exp\left[-2 \int_{z_{lid}}^z \alpha'(z') dr'\right] \quad (3.5)$$

where

$$\alpha'(z) = (\alpha(z) + S(z)\beta_R(z)) \quad (3.6)$$

Eq. (3.7) now has the same form as the simple single-scatter lidar equation in a single component atmosphere. This equation is in fact a differential equation whose solution can be written as

$$\tau'(z_1, z_2) = -0.5 \ln \left[1 - 2 \int_{z_1}^{z_2} B_t(z') dr' \right] \quad (3.8)$$

where $\tau'(z_1, z_2) = \int_{z_1}^{z_2} \alpha'(z') dr'$. Equivalently, in terms of α' the solution can be written as

$$\alpha'(z) = \frac{B_t(z)}{\frac{B_t(z_m)}{\alpha'(z_m)} - 2 \int_{z_m}^z B_t(z') dr'} \quad (3.9)$$

where z_m is some boundary range where $\alpha'(z_m)$ is prescribed. Using Eq. (3.5) the boundary value term can be expressed as

$$\frac{B_t(z_m)}{\alpha'(z_m)} = \exp \left[-2 \int_{z_m}^{z_{lid}} \alpha'(z') dr' \right] \quad (3.10)$$

If z_m is chosen to be an altitude high enough so that no non-negligible amounts of aerosol/cloud exist between z_m and z_{lid} we can write

$$\frac{B_t(z_m)}{\alpha'(z_m)} = \exp \left[-2 \int_{z_m}^{z_{lid}} S(z') \beta_R(z') dr' \right] \quad (3.11)$$

Thus, if profiles of $M(z)$ and $S(z)$ are specified¹, then Eqns. (3.9) and (3.11) can then be used to estimate the extinction profile. In the next section (Section 3.3.1) we will show how using the Rayleigh signal provides a means whereby suitable profiles of $S(z)$ may be estimated. In Section 3.3.2 the methods used to account for multiple-scattering used in this work are described. Further, a well-know difficulty associated with “forward-inversions” (i.e. $z < z_m$ in Eq. (3.9)) is that seemingly small calibration errors and/or small inaccuracies in $S(z)$ can often lead to unphysical and

¹ Note that for altitudes where we expect $\alpha(z)$ to be small compared to $\beta_R(z)$ (i.e. on the basis of an It input Target Mask) then the corresponding values of $S(z)$ can be set to any non-zero constant (in this work we use 1) and the derivation presented here remains valid.

unstable inversions results. How this difficulty may be surmounted is described in Section 3.3.7.

3.3.1 Use of the Rayleigh Channel

Up to this point we have used only the total backscatter signal. Using the Rayleigh channel gives us a means, in effect, to help constrain the values of $S(z)$ necessary in order to apply Eqn.(3.9). In particular, we seek to find the profile of $S(z)$ that allows us (with the additional aid of a suitable multiple-scattering model to estimate $M(z)$) to accurately forward model the Rayleigh signal. In broad terms, the general approach that this retrieval procedure embodies is schematically shown in Figure 2.

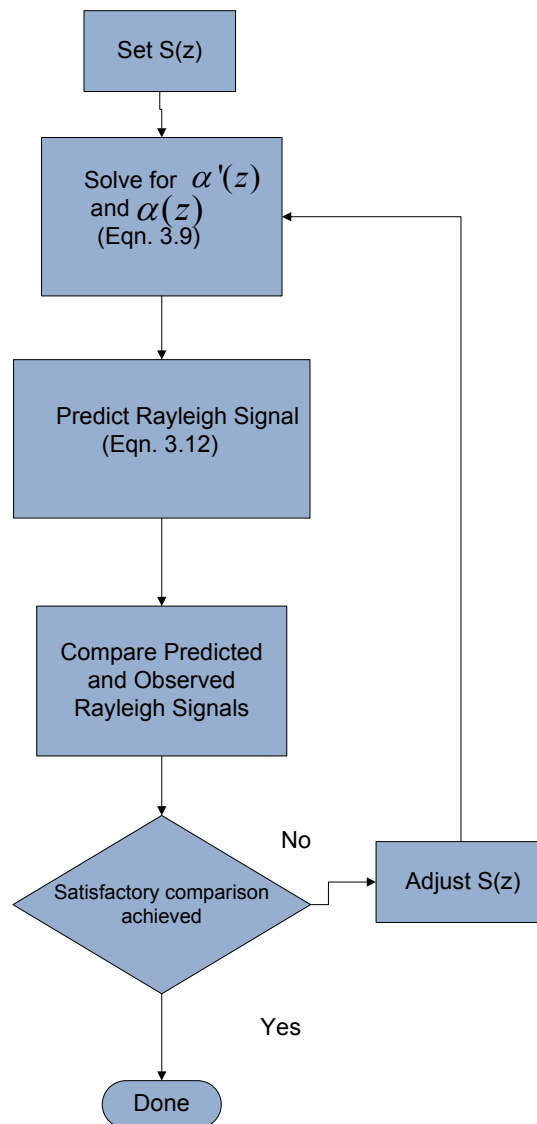


Figure 2: High level simplified schematic of the core approach of the algorithm Note that within this diagram multiple-scattering is not explicitly treated.

The forward model for the (calibrated) Rayleigh signal can be written as

$$\begin{aligned}
 p_R(z) &= \frac{(\beta_R(z))}{r(z)^2} \frac{1}{M_R(z)} \exp\left[-2 \int_{z_{lid}}^z (\alpha_M(z') + \alpha_R(z')) dr'\right] \\
 &= \frac{(\beta_R(z))}{r(z)^2} \frac{1}{M_R(z)} \exp\left[-2(\tau_R(z) + \tau'(z) - \tau_\beta(z))\right]
 \end{aligned} \tag{3.12}$$

where $\tau_R(z) = \int_0^z \alpha_R(z') dz'$, $\tau_\beta(z) = \int_0^z S(z') \beta_R(z') dz'$, M_R is the multiples scattering factor for the Rayleigh signal (which in general may be different from that appropriate for the Mie channel signal). The Rayleigh scattering and extinction profile are known functions of the laser wavelength and the atmospheric density profile while $\alpha(z')$ is supplied via Eqn. (3.9) together with Eq. (3.6). We note that the depolarization ratio for Rayleigh scattering in the case of EarthCARE where the receiver band-width is small enough such that the Raman wings are excluded is on the order of 0.4% for linearly polarized light. Thus, in this work we assume that $p_R \approx p_R^{co}$.

3.3.2 Multiple Scattering

In general, for lidar cloud remote sensing multiple scattering effects must be taken into account. This is especially true for space-based observations. Monte-Carlo (MC) simulations are highly accurate. However, in general, they are too computationally expensive to use in an inversion procedure. For reasons, that will be described later the algorithm makes use of two different approaches to account for MS effects.

3.3.2.1 Analytical model of Hogan

A fast and reasonably accurate approach is the approach developed by Hogan (2006). Using Hogan's model $M_t(z)$ and $M_R(z)$ can be predicted as functions of the extinction profile and a few other parameters. In particular,

$$M_{t,R} = M_H(\alpha_M(z); R_a(z); \alpha_R(z); \rho_l; \rho_t; r(z)) \tag{3.13}$$

where ρ_l is the laser e^{-1} width, ρ_t is the telescope field-of-view and R_a is the "equivalent area" radius which for a collection of particles each with characteristic size D is defined such that

$$\pi R_a^2 = \alpha^{-1} \int_0^\infty N(D) \sigma(D) A_c(D) dD \tag{3.14}$$

where $N(D)$ is the particle size distribution, σ is the single particle extinction cross-

section and A_c is the particle cross-sectional area. For further details of Hogan’s model the reader is referred to Hogan [2006].

Hogan’s model can be used to predict $M(z)$ in Eq.(3.3) so that $b_i(z)$ can be defined. Then, with an assumed $S(z)$ profile and boundary value Eqn. (3.9) can be solved to yield the extinction profile. However, $M_i(z)$ is itself a function of the extinction profile. Thus, the solution of the system must proceed iteratively. $M_R(z)$, which is related to $M_i(z)$ by a multiplicative, constant is used in Eq.(3.12) to account for the effect of MS on the Rayleigh channel.

A sample comparison between Hogan’s model and exact MC results is shown in Figure 3. Here, by comparing the total return and the single-scatter only return that MS effects are significant. Further, it can be seen that, the influence of particle size within the cloud is limited. However, the Rayleigh scattering “tail” under the cloud is sensitive to the cloud particles sizes.

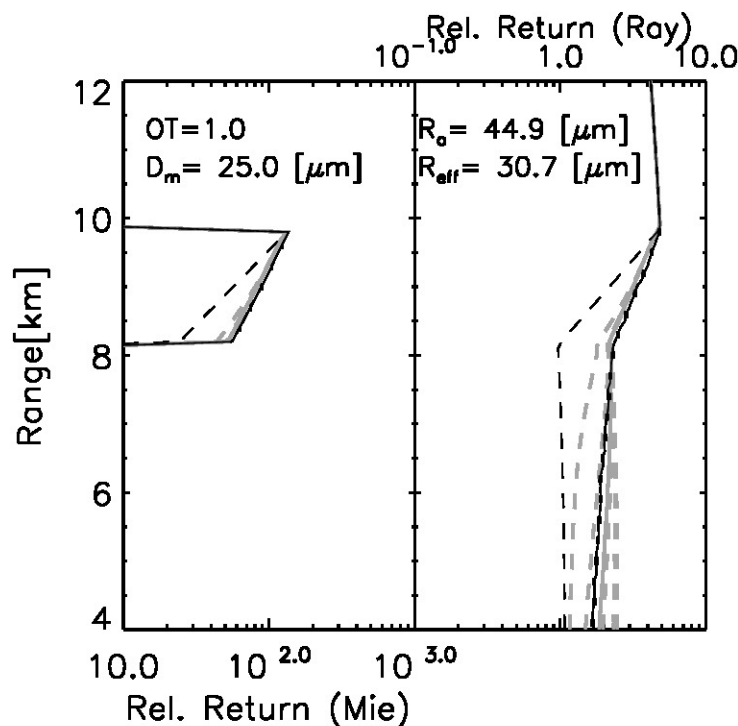


Figure 3. Sample comparison between the ECSIM lidar Monte-Carlo multiple scattering model and the analytical model due to Hogan (2006). (Left) Mie co-polar and (Right) Rayleigh channel co-polar returns for an ice cloud of OT 0. and an effective radius of 30.7 microns. Black solid: ECSIM results. Dashed Black: Single scattering results. Solid Grey: Hogan's model results for the true value of R_a . Dashed Grey from left to right: Hogan's model results for $R_a=10, 25.0, 50, 100$ and 200 microns respectively.

Hogan’s approach is orders of magnitude faster than MC calculations. However, it is still much slower than the corresponding single-scattering case. Moreover, we also require an efficient means to initialize $M(z)$ when solving Eq. (3.9).

3.3.2.2 Platt's approach

Within Figure 3, it can also be noted that, within the cloud, that the observed signal closely resembles a less attenuated version of the single-scattering signal. This is to be expected when the particles are large compared to the wavelength of the laser light so that half the scattered energy is scattered forward in a narrow diffraction lobe and largely stays within the lidar receiver file-of-view. This result was noted by Klett (1973) and forms the basis of a simple method for accounting for Multiple-scattering effects.

If we define

$$M_p(z) = \exp \left[-2 \int_0^z ((1 - \eta(z)) \alpha_M(z) dr' \right] \quad (3.15)$$

where η is the Platt coefficient which physically describes the fraction of scattered energy that remains within the lidar filed-of-view (and thus behaves like it has not be scattered). Approximating $M_t(z)$ by $M_p(z)$ in Eq.(3.1) gives

$$p_t(z) = \frac{(\beta_M(z) + \beta_R(z))}{r(z)^2} \exp \left[-2 \int_{z_{lid}}^z (\eta(z') \alpha_M(z') + \alpha_R(z')) dr' \right] \quad (3.16)$$

Using a similar procedure as used to derive Eqns.(3.8)- (3.10) it can be shown that Eqns.(3.8)- (3.10) apply if the following substitutions are made:

- $S(z) \rightarrow S(z)\eta(Z)$
- $\alpha(z) \rightarrow \eta(z)\alpha(z)$
- $M_t(z) \rightarrow 1$.

It is important to note that in this case the solution, accounting for MS effects, is obtained in one step. No iteration is then required to account for MS effects.

Compared to the approach of Hogan, Platt's approach is faster and simpler but is limited. In Figure 4, a comparison between a MC calculation, the results of Hogan's model and Eq.(3.16) are shown. Here it can be seen that, within the cloud Platt's approach performs well. However, under the cloud Platt's approach cannot capture the decaying structure of the "tail".

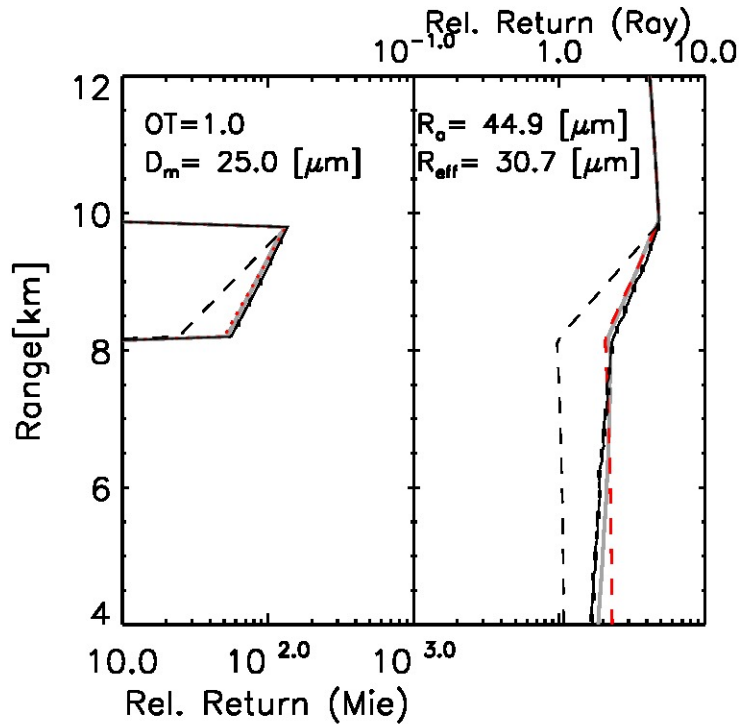


Figure 4: As Figure 3, however the results for Hogan’s model are shown only for $R_a=25.0$ microns and the Red lines shown the result of predicting M using Eq. (3.15) with $\eta=0.55$.

Taking into account the strengths and weaknesses of both approaches we make use of both approaches in this work. In particular, we first solve the system outlined in Figure 2 using Platts’ approach to invert the total signal profile but using Hogan’s approach to predict $M(z)$ for use in forward modelling the Rayleigh signal profile. After convergence we then we compare the effective $M(z)$ profiles predicted by Eq. (3.15) and the profile predicted using Hogan’s approach. If significant enough deviation is found, then we update the $M_i(z)$ profile used in the inversion step using Hogan’s model and solve the system again. This procedure is then iterated until appropriate convergence is obtained. This procedure is sketched out schematically in Figure 5.

The combination of the use of both Platt’s approach and Hogan’s approach within a single algorithm may strike one as introducing needless inconsistencies. However, in a sense, the combination of the two approaches solves the problem of how to initialize $M(z)$ when solving Eq. (3.9). This procedure was found to lead to more stable results, particularly, for higher optical depths than a procedure that relied entirely on Hogan’s model.

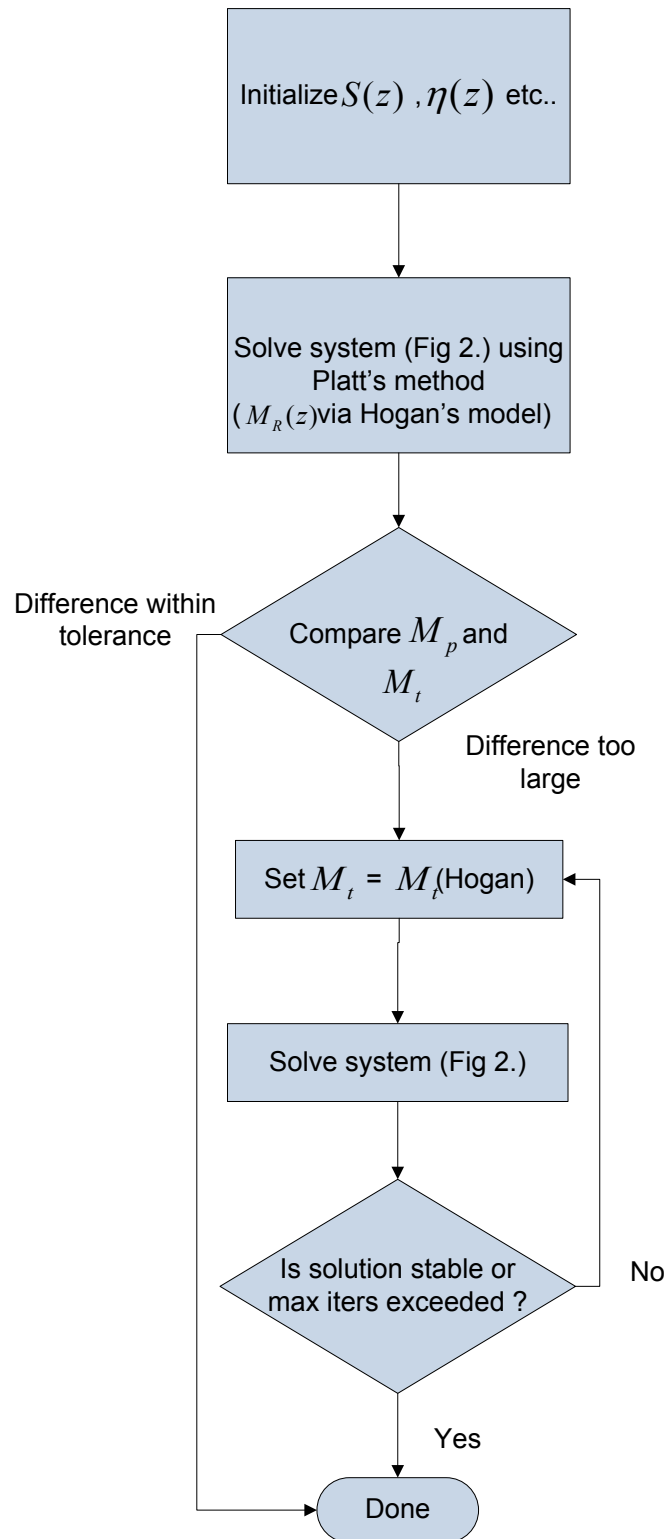


Figure 5: High level schematic describing how Multiple Scattering is accounted for in this algorithm.

3.3.3 Construction of Total Signal and Cross-Talk effects.

The extinction algorithm makes use of the total signal and the Rayleigh signal. However, the total signal is not available as an L1 input. Instead we must construct it from the available input L1 signal products. In addition, it is desirable to build into the algorithm a degree of tolerance in the calibration and cross-talk correction procedure used at the L1 stage. In addition to providing a potentially more accurate product, this will also enable us to provide an independent check at the L2 product level of the L1 signal products. To limit the complexity of the procedure will not however consider the effects of polarization cross-talk effects (which are second-order when compared to the Rayleigh-Mie cross talk effects) and will assume they are perfectly corrected for at the L1 level.

For ATLID, due to the imperfect separation of the co-polar Rayleigh and Mie channels the relationship between the 'observed' signals and the 'true or X-talk corrected and calibrated' Mie and Rayleigh co-polar signals can be expressed as

$$p_{o,M}^{co}(z) = C_M p_M^{co}(z) + X(z) C_R p_R^{co}(z) \quad (3.17)$$

$$p_{o,R}^{co}(z) = E C_M p_M^{co}(z) + C_R p_R^{co}(z) \quad (3.18)$$

where the 'o' subscripts are used to denote the observed (cross-talk affected) quantities. E is the Rayleigh spectral crosstalk parameter, X is the Mie crosstalk parameter, C_M is the Mie co-polar lidar constant and C_R is the Rayleigh co-polar lidar constant. This system can be inverted to yield

$$p_R^{co}(z) = \left(\frac{1}{C_R} \right) \frac{p_{o,R}^{co}(z) - E p_{o,M}^{co}(z)}{1 - EX(z)} \quad (3.19)$$

and

$$p_M^{co}(z) = \left(\frac{1}{C_M} \right) \frac{p_{o,M}^{co}(z) - X(z) p_{o,R}^{co}(z)}{1 - EX(z)}. \quad (3.20)$$

Thus, the total signal (including the cross polar total return) can be written as

$$p_t(z) = \frac{\left(\left(\frac{1}{C_R} - \frac{X(z)}{C_M} \right) p_{o,M}^{co} + \left(\frac{1}{C_M} - \frac{E}{C_R} \right) p_{o,R}^{co} \right)}{(1 - EX(z))} + \frac{p_{o,t}^{cr}(z)}{C_{cr}} \quad (3.21)$$

where $p_{o,t}^{cr}$ is the observed total cross polar return signal and C_{cr} is the cross-polar lidar calibration constant such that $p_t^{cr} = C_{cr}^{-1} p_{o,t}^{cr}$.

In this work we allow for a degree of uncertainty in the applied cross-talk coefficients by introducing multiplicative adjustment factors ($f_{C_M}, f_X, f_E, f_{C_R}, f_{C_{cr}}$) for the cross-talk and calibration coefficients such that the *adjusted total signal* is given by

$$p_i^f(z) = \frac{\left(\left(\frac{1}{f_{C_R} C_R} - \frac{f_X X(z)}{f_{C_M} C_M} \right) p_{o,M}^{co} + \left(\frac{1}{f_{C_M} C_M} - \frac{f_E E}{f_{C_R} C_R} \right) p_{o,R}^{co} \right)}{(1 - f_E E f_X X(z))} + \frac{p_{o,t}^{cr}(z)}{f_{C_{cr}} C_{cr}} \quad (3.22)$$

Note here that the adjustment factors are not-range dependent. Similarly the equation for the *adjusted* Rayleigh channel calibrated backscatter signal becomes

$$p_R^{co,f}(z) = \left(\frac{1}{f_{C_R} C_R} \right) \frac{p_{o,R}^{co}(z) - f_E E p_{o,M}^{co}(z)}{1 - f_E E f_X X(z)} \quad (3.23)$$

3.3.4 Horizontal Signal binning

Due to the non-linear relationship between the lidar signal and the extinction care must be taken when averaging the signal. In particular, averaging signal profiles with large differences in extinction profiles will result in inaccurate inversions. Thus, in this work we attempt to average only similar signal profiles together before applying the inversion procedure.

This strategy is schematically depicted within Figure 6. The bold boxes correspond to the nominal L2 output resolution (1-km). Here “strong” features identified by an input target mask are used to identify sub-groups within the L2 output grid. The cloud/aerosol properties such as S , η and R_a are assumed to be horizontally homogeneous within each nominal L2 output domain only the extinction (and backscatter) itself is allowed to vary horizontally between sub groups.

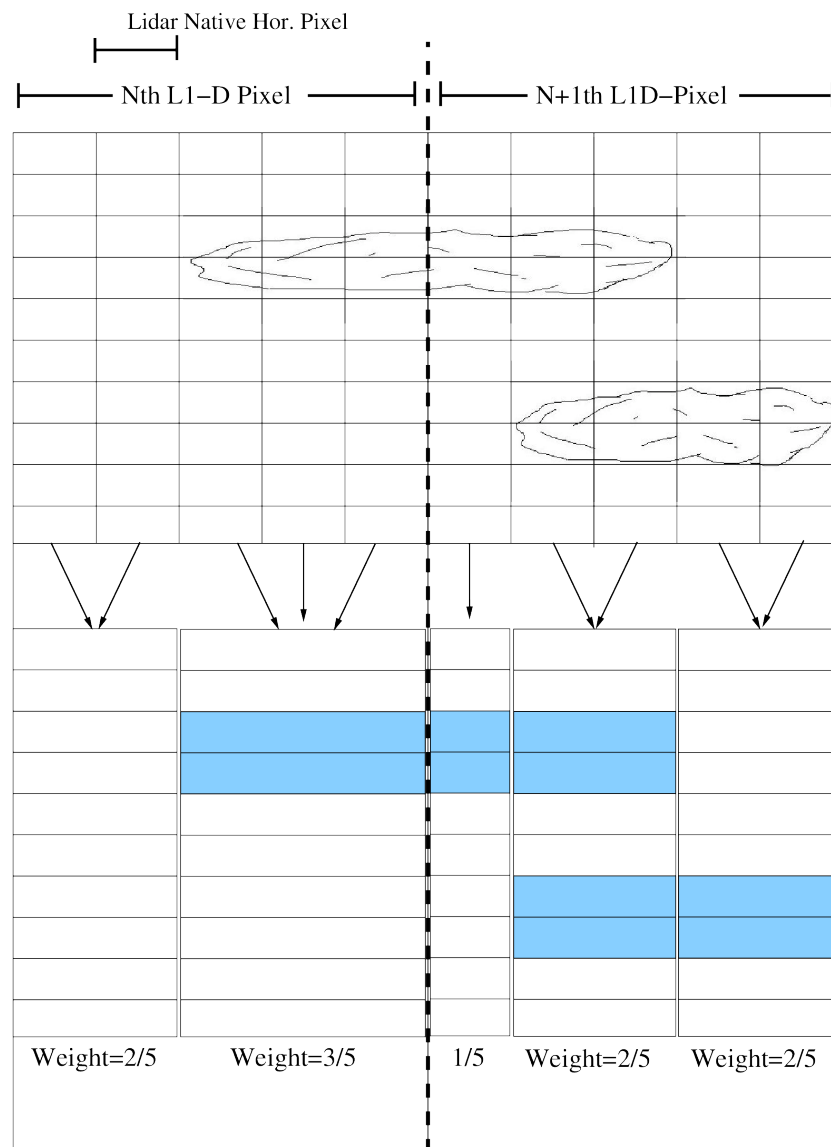


Figure 6: Schematic depiction of the horizontal averaging strategy employed within this algorithm.

3.3.5 Optimal Estimation procedure.

Here we will discuss the means by which we will achieve our goal of solving Eq. (3.9) such that the Rayleigh signal predicted by Eq.(3.12) matches the observed Rayleigh signal (i.e. solving the system depicted in Figure 2).

In this work we employ the principle of Optimal Estimation [Rodgers 2000]. In general terms, we formulate a cost-function that characterizes the likelihood of the measurements being what they were given a particular parameter configuration of an appropriate forward model combined with our expectations concerning the forward-model parameters. The desired solution is then obtained by minimizing this function.

Our cost function can be written as

$$\chi^2 = \sum_{i_g=1}^{n_g} \left([\mathbf{y}_{i_g} - \mathbf{F}_{i_g}(\mathbf{x})]^T \mathbf{S}_{e,i_g}^{-1} [\mathbf{y}_{i_g} - \mathbf{F}_{i_g}(\mathbf{x})] \right) + \left[\exp \left[\mathbf{abs}(\ln(\mathbf{x}^f)) \right] - \mathbf{x}_a^f \right]^T \mathbf{S}_a^{f-1} \left[\exp \left[\mathbf{abs}(\ln(\mathbf{x}^f)) \right] - \mathbf{x}_a^f \right] \quad (3.24)$$

the i_g subscripts denote the sub-group as described in Section 3.3.4 above and:

1. \mathbf{y}_{i_g} is the *observation vector* (related to the actually observed signal via Eq.(3.23))

$$\mathbf{y}_{i_g} = (p_{R,i_g}(z_1), p_{R,i_g}(z_2) \dots p_{R,i_g}(z_{nz}))^T \quad (3.25)$$

2. \mathbf{x} is the *state-vector* and \mathbf{x}^f is the *normalized state-vector*. Here defined such that

$$\mathbf{x}^f = (f_{C_M}, f_X, f_E, f_{C_R}, f_{C_{cr}}, f_{R_a,1} \dots f_{R_a,1}, f_{S,n_l} \dots f_{S,n_l}, f_{\eta,1} \dots f_{\eta,n_l})^T \quad (3.26)$$

where n_l is the number of layers used in the retrieval. In this work we have chosen to cast the problem in terms of normalized variables (the f_{R_a}, f_{η}, f_S 's) such that

$$\mathbf{x} = \mathbf{x}^f \mathbf{x}_a \quad (3.27)$$

(here multiplication between two column or two row vectors is assumed to be element-wise) where \mathbf{x}_a is the *a priori* matrix

$$\mathbf{x}_a = (C_M^a, X^a, E^a, C_R^a, C_{cr}^a, R_{a,1}^a \dots R_{a,n_l}^a, S_{1,1}^a \dots S_{n_l,n_l}^a, \eta_{1,1}^a \dots \eta_{n_l,n_l}^a)^T \quad (3.28)$$

where, for simplicity, we have written, the expressions for the state and a priori vectors corresponding to the case where the cross-talk associated elements are not range-dependent.

3. $\mathbf{F}(\mathbf{x})$ is the forward model (Eq.(3.12)).
4. \mathbf{S}_e is the observation error covariance matrix. Using Eqn.(3.19) and the fact that the observed signals are uncorrelated gives

$$[S_e]_{i,j} = \begin{cases} \left(\frac{1}{K_R}\right)^2 \frac{\sigma_{p_{o,R}}^2(z) + E^2 \sigma_{p_{o,M}}^2(z)}{(1-EX(z))^2} & i = j \\ 0 & i \neq j \end{cases} \quad (3.29)$$

The relationship between the variances in the above equation and the reported L1 error information is described later in Section 5.5.2.

5. S_a^f is the a priori error covariance matrix corresponding to the normalized variables.
6. x_a is the a priori state vector corresponding to the normalized variables so that, by definition, $x_a^f = (1,1,1,\dots,1)$

It may be noted that the form of the cost function related to the distance from the a priori is somewhat non-standard. This has to do with the choice of working in terms of x^f instead of using x . Using x^f insures that that all the minimization variables are scaled to the same magnitude which aids in the numerical minimization process. The second reason has to do with the nature of the state-variables themselves and their variances. It is more physically reasonable to express the a priori distribution of S and R_a in a multiplicative rather than linear sense. For example, observations show that S for a certain aerosol type is more accurately characterized by stating $20 \times / \div 0.5$ (giving a 1-sigma range in this case of 10-40) rather than say 20 ± 20 (giving a 1-sigma range in linear space of 0-40). Our choice of functional form for the a priori component of the cost function reflects this. In fact, the form of the second component in Eqn. (3.24) is consistent with assuming that the components of the state normalized vector $[x^f]_i$ are distributed such that

$$p(x_i^f) = \frac{1}{\sqrt{2\pi\sigma_{x_i^f}^2}} \exp\left[-\left(\frac{x_i^f-1}{2\sigma_{x_i^f}}\right)^2\right] \quad f_i \geq 1$$

$$p(x_i^f) = \frac{1}{\sqrt{2\pi\sigma_{x_i^f}^2}} \exp\left[-\left(\frac{\frac{1}{x_i^f}-1}{2\sigma_{x_i^f}}\right)^2\right] \quad f_i < 1 \quad (3.30)$$

so that, for example, the probability that $[x^f]_i = 2.0$ is the same as for $[x^f]_i = 1/2$.

A comparison between the PDF described by Eqn. (3.30) and two more conventional formulations is shown in Figure 7. Here Eqn. (3.30) is compared to the case where $\ln(x^f)$ is assumed to be Gaussian and the case where x^f is Gaussian. Here it can be seen that Eqn. (3.30) is equivalent to the case where x^f is Gaussian if $x^f > 1$. However, in the case where x^f is Gaussian negative values of x^f are allowed which is unphysical. Comparing Eqn. (3.30) to the case where $\ln(x^f)$ is assumed to be Gaussian it can be seen that they both do not allow negative values and they are similar for values of x^f between about 0.5 and 1.5. However, outside of this range,

Eqn. (3.30) yields much lower probabilities.

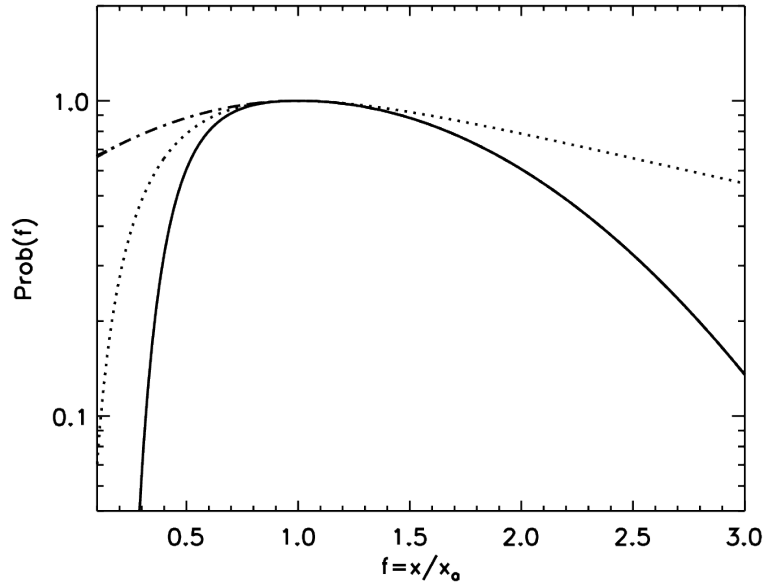


Figure 7: Normalized probability as a function between the ratio of a variables value to its expected value for (solid-line) Eqn. (3.30), (dotted-line) $\ln(x^f)$ is assumed to be Gaussian (dash-dotted) case where x^f is Gaussian. Note that for x-axis values greater than one that the solid and dash-dotted lines overlap. For all lines it has been assumed that $\sigma_{x^f}^2 = 1$.

3.3.6 Determination of inversion layers and Specification of a priori values

In order to minimize Eqn. (3.24), the a priori values of S_a^F and x_a must be specified. This procedure is linked to the determination of the inversion layers. Each output resolution volume is classified as being ice cloud, water cloud or aerosol on the basis of the backscatter, extinction and the depolarization ratio. In addition the temperature and the estimated boundary layer height from a suitable operational analysis are used. For the volumes identified as being 'aerosols' the classification is then refined using the aerosol classification algorithm. The classification procedures are algorithms in their own right and are described in detail in a separate ATBD [A-TC-ATBD].

Once the classification, including aerosol typing, has been achieved then the inversion layers are determined. These layers are determined both on the basis of the Target Mask and the Classification products. This process is described in Sections 5.5.1.4 and 5.5.1.5 (see also [A-TC-ATBD]). State variables are assumed to be uncorrelated between different inversion layers.

For layers classified as aerosol, the a priori values are generated using the output of the *large-scale aerosol-only backscatter, extinction and depolarization ratio product* [A-AER-ATBD] together with the output of the aerosol classification algorithm. Corresponding a priori values of R_a and η are based directly on the aerosol type while in the case of the extinction-to-backscatter they are computed from the quantitative large-scale extinction-backscatter product. In particular, for a given layer

extending in altitude between z_l and z_u we have

$$S_a = \frac{\langle \alpha_{ls} \rangle}{\langle \beta_{ls} \rangle} = \frac{\sum_{i=l}^u \alpha_{ls}(z_i)}{\sum_{i=l}^u \beta_{ls}(z_i)} \quad (3.31)$$

where the ls subscript is used to denote products generated by the large-scale aerosol-only algorithm and the brackets denote averaging. We assume that the large scale extinction and backscatter products are uncorrelated so that the corresponding variance in S_a is then

$$\sigma_{S_a}^2 = S_a^2 \left(\frac{\sigma_{\langle \alpha_{ls} \rangle}^2}{\langle \alpha_{ls} \rangle} + \frac{\sigma_{\langle \beta_{ls} \rangle}^2}{\langle \beta_{ls} \rangle} \right) \quad (3.32)$$

Since the large-scale extinction product is, in general, strongly correlated in the vertical dimension, the vertical correlation must be taken into account and thus the extinction variance is given by

$$\sigma_{\langle \alpha_{ls} \rangle}^2 = \sum_{i=l}^u \sum_{j=l}^u [C_{\alpha_{ls}}]_{i,j} \quad (3.33)$$

where $C_{\alpha_{ls}}$ is the variance-covariance matrix corresponding to the large-scale extinction product. The variance of the layer averaged backscatter is obtained in a similar manner.

For ice and water clouds separate a priori S, η and R_a a priori values and variances are used. These values are set in the algorithm configuration file.

3.3.7 Optimization procedure

In this work the minimum of the cost function is obtained numerically using a variant of the *Broyden-Fletcher-Goldfarb-Shanno* (BFGS) approach [Press et al. 1992]. The approach follows that described in Press et al. except for the fact that numerical derivatives are used. This was done largely due to save time during the development process. The algorithm speed seems to be sufficient using numerical derivatives. However, the use of analytical derivatives would almost surely result in a faster algorithm and should be considered as part of any future development.

During testing it was found that the minimization procedure too often converged to a spurious local minimum depending in a sometimes sensitive fashion on the initial guess. This behaviour was found not to be a result of the particular minimization procedure used. Rather, this undesirable behaviour was traced to the well-know forward inversion instability which is a characteristic of equations similar in form to Eq.(3.9). In particular, when the denominator becomes small numerical forms of Eq. (3.9) can generate large almost random values of α . This, in turn leads to a large

amount of spurious structure being present in Eqn. (3.24). This is illustrated in Figure 8, where we show results corresponding to a simplified form of (3.24) here it can clearly be seen that for too high values of $\alpha(z_m)$ and S the cost function is no longer smooth and possesses a complicated structure.

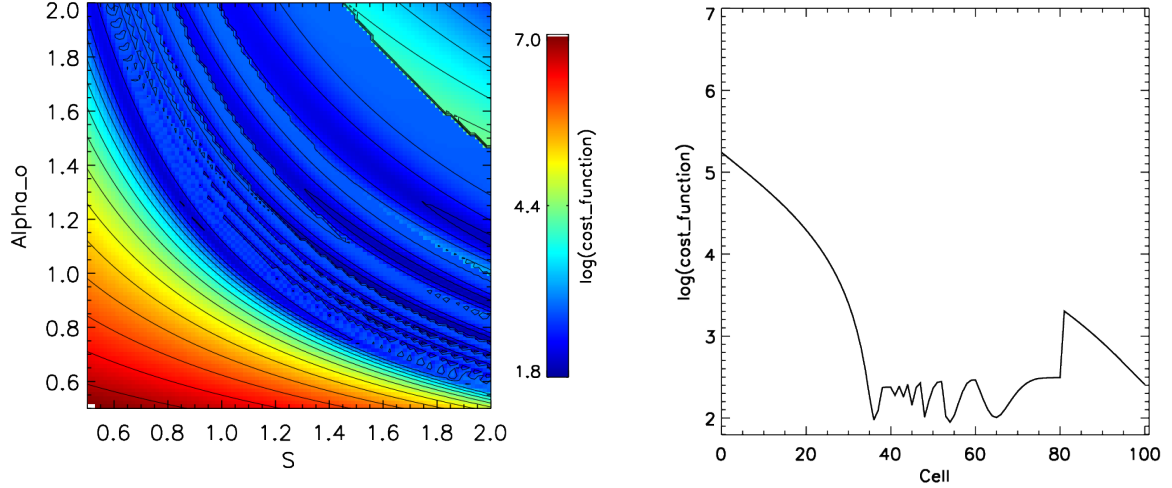


Figure 8: Left: Simplified Cost function as a function of normalized values of $\alpha(z_m)$ and S . Right: sample cross section through the data shown in the Left panel. Conditions correspond to a single layer cloud with an optical depth of 1.5. No multiple-scattering effects were considered.

Several strategies to avoid the behaviour of the type shown in Figure 8 above were investigated. It was found modifying cost function the adding a penalty term based on the value of the denominator in Eq.(3.9) was found to be an effective solution. Thus in this work the cost function that is actually minimized is

$$\chi'^2 = \chi^2 + \chi_{pen}^2 \quad (3.34)$$

The penalty function χ_{pen}^2 is defined as

$$\begin{aligned} \chi_{pen}^2 &= \lambda_{pen} \text{Min}[\text{Den}(z_i)]^2 & : \text{Min}[\text{Den}(Z_i)] < 0 \\ &= 0 & : \text{Min}[\text{Den}(Z_i)] \geq 0 \end{aligned} \quad (3.35)$$

where

$$\text{Den}(z) = \frac{B_t(z_m)}{\alpha'(z_m)} - 2 \int_{z_m}^z B_t(z') dr' \quad (3.36)$$

(which is the just the denominator in Eqn.(3.9)). λ_{pen} should be set to a value very much larger than the expected minimum value of χ^2 (a value of 10^4 is used throughout this work).

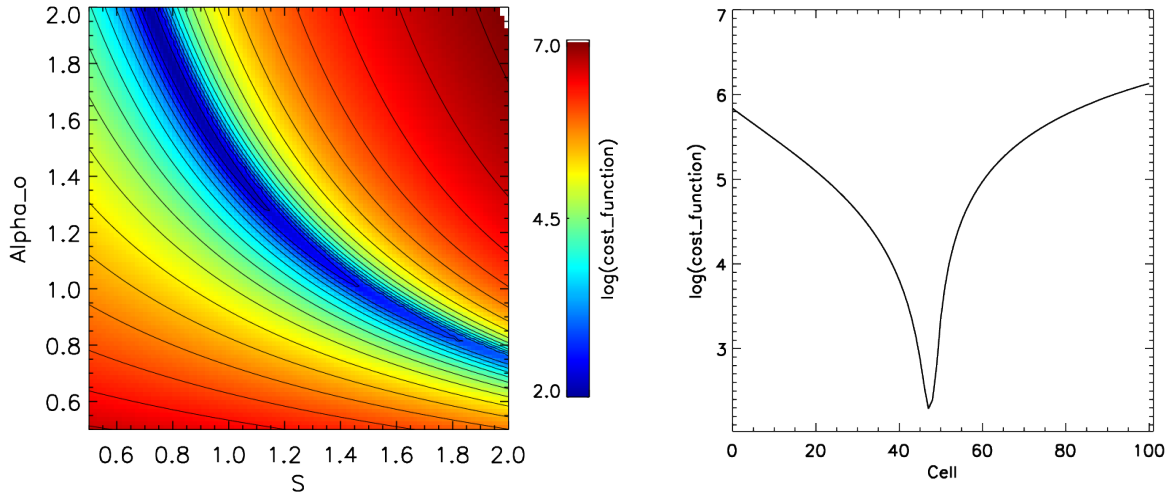


Figure 9: Left: Simplified Cost function with the penalty term added shown as a function of normalized values of $\alpha(z_m)$ and S . Right: sample cross section through the data shown in the Left panel. Conditions correspond to a single layer cloud with an optical depth of 1.5. No multiple-scattering effects were considered.

The effect of adding the penalty term is illustrated in Figure 9 above. Compared to the previous figure the cost function penalty term effectively eliminates the spurious structure present in the unmodified cost function.

3.3.8 Error Estimates

Following Press et al., the formal covariance matrix of the retrieved state-vector can be derived from the curvature-matrix

$$\mathbf{C} = \frac{1}{2} \left[\frac{\partial^2 \chi^2}{\partial x^f_i \partial x^f_j} \right]^{-1} \quad (3.37)$$

where the partial derivatives are taken at the minimum point. Applied to Eqn. (3.24), this will yield the covariance matrix for the cross-talk parameters, the extinction-to-backscatter ratios, and the R_a 's.

The variances and covariances involving the retrieved extinction values and optical thicknesses are then derived using the state-vector covariance matrix and the signal error estimates appropriately combined with the partial derivatives of the extinction and optical thickness with respect to the state variables and the signals themselves. More details are given in Section 5.5.7.

4 Justification for the selection of the algorithm

The choice of the approach described in this ATBD can be justified on the basis of the following points.

The algorithm fulfils the appropriate requirements. Namely, it produces estimates of the extinction profile, the backscatter profile and the depolarization on a horizontal scale of 1-km.

Both the information in the Rayleigh and in the Mie channel is utilised. This improves the accuracy of the algorithm. The basic philosophy used by the algorithm in order to optimally combine the information present in both channels of the algorithm can easily be connected to well-established lidar techniques. Namely, the essence of the algorithm described in this ATBD, is to perform a Klett-like retrieval using an S profiles which yields an extinction profile which, in turn, enables an optimal reconstruction of the observed Rayleigh channel signal

By using a Klett-like inversion step the number of variables in the state-vector is reduced, leading to a faster algorithm.

Use of an optimal estimation framework allows for the derivation of a consistent complete set of errors and error covariances.

5 Mathematical algorithm Description

5.1 Input parameters

Variable	Symbol	Description	Source	Unit	Dim	Type
Time	t	UTC time	ATLID-L1b	s	time	real*8
L1-D (x-z)_Common_Grid	?	?	?	?	?	?
sampleAltitudes	Z	Average height of each lidar gate above mean sea level	ATLID-L1b	m	time,height	real
sampleRange	RZ	Average range from lidar for each range gate	ATLID-L1b	m	time,height	real
pitchAngle	$\hat{\theta}_{LOS}$	Lidar view angle relative to nadir	ATLID-L1b	deg	time	real
sampleGeoLocLat	ϕ	Latitude of samples	ATLID-L1b	deg	time,height	real
sampleGeoLocLong	λ	Longitude of samples	ATLID-L1b	deg	time,height	real
LayerTemperature	AtmTemp	Atmospheric temperature at sample altitude	ATLID-L1b	K	time,height	real
LayerPressure	AtmPress	Atmospheric pressure at sample altitude	ATLID-L1b	Pa	time,height	real
SpectCrossTalkRay	ϵ	Moving averaged spectral crosstalk parameter for the Rayleigh channel	ATLID-L1b	-	time	real
SpectCrossTalkRayError	σ_{ϵ}	SD of ϵ	ATLID-L1b	-	time	real
SpectCrossTalkMie	χ_{Ref}	Moving averaged spectral crosstalk parameter for the Mie channel	ATLID-L1b	-	time	real

SpectCrossTalkMieError	σ_{χ}	SD of χ_{Ref}	ATLID-L1b	-	time	real
SpectCrossTalkMie	δ_{χ}	Correction applied to χ_{Ref}	ATLID-L1b	-	time,height	real
MIECopolarLidarConstant	\hat{K}_{Mie}^0	Mie copolar lidar constant	ATLID-L1b	-	time	real
MIECopolarLidarConstantError	$errKmie$	Estimate error on \hat{K}_{Mie}^0	ATLID-L1b	-	time	real
RAYCopolarLidarConstant	\hat{K}_{Ray}^0	Ray copolar lidar constant	ATLID-L1b	-	time	real
MIECopolarLidarConstantError	$errKray$	Estimate error on \hat{K}_{Ray}^0	ATLID-L1b	-	time	real
CrosspolarLidarConstant	\hat{K}_{Cro}^0	Crosspolar lidar constant	ATLID-L1b	-	time	real
CrosspolarLidarConstantError	$errKcro$	Estimate error on \hat{K}_{Cro}^0	ATLID-L1b	-	time	real
RAYinp_Signal	Ray_{inp}	Calibrated cross-talk corrected Rayleigh channel backscatter	ATLID-L1b	1/m/sr	time,height	real
MIEinp_Signal	$MieCop_{inp}$	Calibrated cross-talk corrected Mie co-polar channel backscatter	ATLID-L1b	1/m/sr	time,height	real
CROinp_Signal	CRO_{inp}	Calibrated cross-talk corrected cross-polar channel backscatter	ATLID-L1b	1/m/sr	time,height	real
RetrievedSignalError	$ScDataError$	Total error on retrieved signals	ATLID-L1b	1/m/sr	3,time,height	real
PeakTransmissionRatio	\hat{K}_P^{HSR}	Estimation of etalon peak transmission ratio	CCDB	-	time	real

RayReflec	$\tau_{Ray}(T)$	Part of Rayleigh spectrum reflected by the HSR etalon (function of atmospheric temperature)	CCBD	-	time,height	real
RayReflecRef	$\tau_{Ray}(T_{ref})$	Part of Rayleigh spectrum reflected by the HSR etalon at reference temperature	CCDB	-	time	real
PeakTransmissionRatioErr	$errTpeak$	Error on \hat{K}_p^{HSR}	CCDB	-	time	real
RayReflecErr	$errTauR$	Error on $\tau_{Ray}(T)$	CCDB	-	time	real
rho_t	ρ_t	Telescope full-angle filed-of-view	?	mrads	scalar	real
rho_lid	ρ_l	Laser divergence full 1/e width	?	mrads	scalar	real
ext_ls	α_{ls}	Large scale extinction	A-AER-L2a	1/m	time,height	real
D_ext_ls	$\sigma_{\alpha_{ls}}$	Large scale extinction error	A-AER-L2a	1/m	time,height	real
Ret_ERR_COV_MAT_EXT	$C_{\alpha_{ls}}$	Large scale error covariance matrix	A-AER-L2a	1/m ²	time, (height,8), (height,8)	real
beta_ls	β_{ls}	Large scale extinction	A-AER-L2a	1/m/sr	time,height	real
D_beta_ls	$\sigma_{\beta_{ls}}$	Large scale extinction error	A-AER-L2a	1/m/sr	time,height	real
Depol_ls	δ_{ls}	Large scale depolarization ratio	A-AER-L2a	-	time,height	real
D_Depol_ls	$\sigma_{\delta_{ls}}$	Large scale depolarization error	A-AER-L2a	-	time,height	real
FeatureMask	$FeatureMask$	Featuremask	A-FM-L2a	-	time,height	real

Table 1: Required input parameters.

5.2 Input Configuration parameters

Variable	Symbol	Description	Unit	Dim	Type
A priori information					
AP_Water_S_ratio	S_{water}	A priori value for water extinction-to-backscatter ratio.	sr	1	real
Sigma_AP_Water_S_ratio	$\sigma_{S_{water}} / S_{water}$	Related fractional standard deviation	-	1	real
ST_Water_S_ratio	S_{water}^o	Starting value used in minimization process	sr	1	real
AP_Ice_S_ratio	S_{ice}	A priori value for ice extinction-to-backscatter ratio.	sr	1	real
Sigma_AP_Ice_ratio	$\sigma_{S_{ice}} / S_{ice}$	Related fractional standard deviation	-	1	real
ST_Ice_S_ratio	S_{ice}^o	Starting value used in minimization process	sr	1	real
AP_Aerosol_S_ratio	S_{aer}	A priori default value for unclassified aerosol extinction-to-backscatter ratio.	sr	1	real
Sigma_AP_Aerosol_S_ratio	$\sigma_{S_{aer}} / S_{aer}$	Related fractional standard deviation	-	1	real

ST_Aerosol_S_ratio	S_{Aer}^o	Starting value used in minimization process	sr	1	real
AP_Water_Ra	Ra_{water}	A priori value for water area-weighted effective radius	um	1	real
Sigma_Water_Ra	$\sigma_{Ra_{water}} / Ra_{water}$	Related fractional standard deviation	-	1	real
ST_Water_Ra	Ra_{water}^o	Starting value used in minimization process	sr	1	real
AP_Ice_Ra	Ra_{ice}	A priori value for cloud ice area-weighted effective radius	um	1	real
Sigma_Ice_Ra	$\sigma_{Ra_{ice}} / Ra_{ice}$	Related fractional standard deviation	-	1	real
ST_Ice_Ra	Ra_{ice}^o	Starting value used in minimization process	sr	1	real
AP_Aerosol_Ra	Ra_{aer}	A priori default value for unclassified aerosol area-weighted effective radius	um	1	real
Sigma_Aerosol_Ra	$\sigma_{Ra_{aer}} / Ra_{aer}$	Related fractional standard deviation	-	1	real
ST_aer_Ra	Ra_{aer}^o	Starting value used in minimization process	-	1	real
AP_Water_eta	η_{water}	A priori value for Platt MS coefficient for water clouds	-	1	real

Sigma_Water_eta	$\sigma_{\eta_{water}} / \eta_{water}$	Related fractional standard deviation	-	1	real
ST_Water_eta	η_{water}^o	Starting value used in minimization process	-	1	real
AP_Ice_eta	η_{ice}	A priori value for Platt MS coefficient for ice clouds	-	1	real
Sigma_Ice_eta	$\sigma_{\eta_{ice}} / \eta_{ice}$	Related fractional standard deviation	-	1	real
ST_Ice_eta	η_{ice}^o	Starting value used in minimization process	-	1	real
AP_Ice_eta	η_{aer}	A priori default value for Platt MS coefficient for unclassified aerosols	-	1	real
Sigma_Ice_eta	$\sigma_{\eta_{aer}} / \eta_{aer}$	Related fractional standard deviation	-	1	real
ST_aer_eta	η_{aer}^o	Starting value used in minimization process	-	1	real
Parameters related to Feature Mask Processing and Layering Determination					
Lidar_FM_thres	FMT	Threshold to apply to the target mask	-	1	integer
Lidar_FM_thres_	FMT_{St}	Threshold to apply to the target mask to determine strong features	-	1	integer

FM_thres_iwin	$iwin_{FMT}$	Allowed window in vertical pixels between strong features used to determine when a new subgroup is started	-	1	integer
Max_layer_thickness	MLT	Maximum thickness allowed for a layer before starting a new layer.	m	1	real
blind_thres	Th_{bld}	SNR threshold used in process to determine the lidar blind altitude (signal is effectively totally extinguished)	-	1	real
blind_win	Δz_{bnd}	Width of altitude window over which the blind_thres applies	m	1	real
Parameters related to algorithm performance					
Min_tol	-	Tolerance parameter supplied to minimization solver	-	1	real
Max_step	-	Maximum allowed step size in minimization solver	-	1	real
Max_min_iters	-	Maximum number of allowed iterations in minimization routine	-	1	integer

Max_MS_iters	-	Maximum number of MS update loop passes	-	1	integer
Tol_MS_update	-	Tolerance related to MS update loop stopping criteria	-	1	real
Max_n_layers	$N_{l,Max}$	Maximum number of allowed layers	-	1	integer
Parameters related to layer classification (Passed to L2a Classification procedure)					
Max_N_layers	$N_{l,max}$	Maximum number of layers an input layer can be subdivided into	-	-	integer
Beta_Cld_default	β_{thres}	Default backscatter threshold for cloud aerosol separation	1/m/sr	-	real
Beta_Cld_strat	$\beta_{thres, strat}$	Default backscatter threshold for cloud aerosol separation for stratospheric layers	1/m/sr	-	real
Beta_Cld_bl	$\beta_{thres, bl}$	Default backscatter threshold for cloud aerosol separation for stratospheric layers	1/m/sr	-	real
A_Depol_beta	$A_{\delta, \beta}$	Slope parameter of depol-backscatter relationship used to determine ice/water threshold	m	-	real

A_Depol_beta	$B_{\delta,\beta}$	Intercept parameter of depol-backscatter relationship used to determine ice/water threshold	-	-	real
Parameters passed to aerosol classification routine					
N_aerosols	N_aer	Total number of aerosols for which a typing probabilities will be calculated	-	1	integer
The following parameters will be provided for each of the aerosol types defined by N_aer					
Depol_center	δ_0	Depol center of the Gaussian distribution	-	1	real
Depol_var	σ_δ	Gaussian width in the depol direction	-	1	real
Lid_rat_center	S_0	Lidar Ratio center of the Gaussian distribution	-	1	real
Lid_rat_var	σ_S	Gaussian width in the lidar ratio direction	-	1	real
Gauss_theta	θ	Angle of the gaussian orrientation. The angle is defined as the right-handed rotation assuming the depolarization at the x-axis	Deg	1	real

Map_name	Map	Name incl. directory of the external aerosol map	-	1	Char
Strat_trop	Strat_trop	Is this an aerosol species in the troposphere (0) or stratosphere(1)	-	1	integer

Table 2: Algorithm input configuration parameters.

5.3 Output parameters

5.3.1 A-ECB outputs

Table 3: A-EBD Related output parameters

Variable	Symbol	Description	Units	Dim	Type
A-ECB outputs					
Time	t	UTC time	S	time	real*8
Longitude	$LongLID$	Latitude of co-located ATLID footprints at the L1-D collocation altitude	degree	time	real
Latitude	$LatLID$	Latitude of co-located ATLID footprints at the L1-D collocation altitude	degree	time	real
sampleAltitudes	Z	Average height of each lidar gate above mean sea level	M	time,height	real
sampleRange	RZ	Average range from lidar for each range gate	M	time,height	real
pitchAngle	$\hat{\theta}_{LOS}$	Lidar view angle relative to nadir	deg	time	real
sampleGeoLocLat	ϕ	Latitude of samples	deg	time,height	real
sampleGeoLocLong	λ	Longitude of samples	deg	time,height	real
num_paras	N_p	Number of state-variable parameters	-	time	integer
num_layers	N_l	Number of layers	-	time	integer
Target_type	TT	Target Classification	-	time,height	integer
MSF	M_t	Multiple scattering correction factor	-	time,range	real
Ray_Beta	β_R	Rayleigh scattering profile	1/m/sr	time,range	real
Ext	α	Extinction	1/m	time,height	real
D_ext	$\sigma_\alpha^{1/2}$	1-sigma-estimated error	1/m	time,height	real
Beta	β	Backscatter	1/m/sr	time,height	real
D_Beta	$\sigma_\beta^{1/2}$	1-sigma-estimated error	1/m/sr	time,height	real

Variable	Symbol	Description	Units	Dim	Type
A-ECB outputs					
S	S	Extinction-to-backscatter ratio	sr	time,Height	real
D_S	$\sigma_S^{1/2}$	1-sigma-estimated error	sr	time,Height	real
Depol	ρ	Depolarization Ratio	-	time,height	real
D_Depol	$\sigma_\rho^{1/2}$	1-sigma estimated error	-	time,height	real
Tau	τ	Cloud-aerosol optical depth	-	time,height	real
D_Tau	$\sigma_\tau^{1/2}$	1-sigma estimated error	-	time,height	real
Ra	R_a	Effective equivalent area radius	microns	time,height	real
D_Ra	$\sigma_{R_a}^{1/2}$	1-sigma-estimated error	microns	time,height	real
State_fx	\mathbf{x}_f	Optimized state vector	-	time,num_paras	real
Cov_State_fx	\mathbf{S}_x^f	Error Covariance Matrix	-	time,num_paras, num_paras	real
State_X_ap	\mathbf{x}_a	A priori state vector	various	time,num_paras	real
D_State_fx_ap	\mathbf{S}_a^f	A priori state vector uncertainty (diagonal elements only)	-	time,num_paras	real
State_fx_fg	\mathbf{x}_0	A priori state vector minimization starting value	-	time,num_paras	real
Sig_tot	p_{tot}	Total attenuated backscatter produced by minimization procedure	1/m/sr	time,range	real
D_Sig_tot	$\sigma_{p_{tot}}^{1/2}$	1-sigma-estimated error	1/m/sr	time,range	real
Sig_mie	$p_{o,M}$	Mie attenuated backscatter produced by minimization procedure	1/m/sr	time,range	real
D_Sig_Mie	$\sigma_{p_{o,M}}^{1/2}$	1-sigma-estimated error	1/m/sr	time,range	real
Sig_Ray	$p_{o,R}$	(Observed) Rayleigh attenuated backscatter produced by minimization procedure	1/m/sr	time,range	real
D_Sig_Ray	$\sigma_{p_{o,R}}^{1/2}$	1-sigma-estimated error	1/m/sr	time,range	real
Pred_Ray_sig	p_R	Predicted Rayleigh attenuated backscatter produced by minimization procedure	1/m/sr	time,range	real
D_Pred_Ray_Sig	$\sigma_{p_R}^{1/2}$	1-sigma-estimated error	1/m/sr	time,range	real
Layer_tops	z_{top}	Layer tops	M	time,N_layers	real
Layer_bots	z_{bot}	Layer bottoms	M	time,N_layers	real
Int_Atten_Beta	$I_{p_{tot}}$	Layer integrated attenuated backscatter	1/sr	time,N_layers	real

Variable	Symbol	Description	Units	Dim	Type
A-ECB outputs					
D_Int_Atten Beta	$\sigma_{I\rho_{tot}}^{1/2}$	1-sigma-estimated error	1/m/sr	time,range	real
Int_Beta	$I\beta_{tot}$	Layer integrated backscatter	1/sr	time,N_layers	real
D_Int_Beta	$\sigma_{I\beta_{tot}}^{1/2}$	1-sigma-estimated error	1/m/sr	time,range	real
Int_Depol	$I\rho$	Layer average depolarization	-	time,N_layers	real
D_Depol	$\sigma_{I\rho}^{1/2}$	1-sigma-estimated error	-	time,range	real
D_B_D_b	$\frac{\partial B_t}{\partial b_t}$	Used to relate MS corrected and S adjusted signals to the standard attenuated backscatter.	sr	time,range	real
D_alpha_D_X	$\left(\frac{\partial\alpha(z)}{\partial X}\right)$	Extinction Jacobian	various	time,range,num_paras	real
D_beta_D_X	$\left(\frac{\partial\beta(z)}{\partial X}\right)$	Backscatter Jacobian	various	time,range,num_paras	real
D_tau_D_X	$\left(\frac{\partial\tau(z)}{\partial X}\right)$	Optical depth Jacobian	various	time,range,num_paras	real
red_Chisq_obs	$\frac{\chi_{o,red}^2}{\nu}$	Reduced Chi-squared goodness of fit parameters for first (observational) component of the cost function ($\nu = (N_z N_g - N_p - 1)$)	-	time	real
red_Chisq_ap	$\frac{\chi_{ap,red}^2}{\nu}$	Reduced Chi-squared goodness of fit parameters for the second (a priori) component of the cost function	-	time	real
red_Chisq_ped	$\frac{\chi_{pen,red}^2}{\nu}$	Reduced Chi-squared goodness of fit parameters for third (penalty) component of the cost function	-	time	Real
Algorithm convergence related variables					
N_MS_Loops	-	Number of loops in MS correction loop	-	time	integer
N_calls	-	Total number of function calls	-	time	integer
Converge_fail	-	0 → Solver converged 1 → Maximum number of iteration reached with no convergence	-	time	integer

5.3.2 A-TC associated outputs

Table 4: A-TC associated outputs

Variable	Symbol	Description	Units	Dim	Type
Time	<i>t</i>	UTC time	S	time	real
Latitude	<i>LatLID</i>	Latitude of co-located ATLID footprints at the L1-D collocation altitude	degree	time	real
Longitude	<i>LongLID</i>	Longitude of co-located ATLID footprints at the LID co-location altitude	degree	time	real
Height	<i>z</i>	Height above mean sea level	m	height	real
surface_altitude	<i>zsurf</i>	Height of surface above mean sea level	m	time	real
lidar_detection_status	<i>DStat_Lid</i>	0 = lidar not working 1 = ground detected 2 = totally extinguished 3 = clear 4 = target detected 5 = molecular 6 = don't know	-	time, height	byte

Target Classification information

The variables describing the classification of the atmosphere by type are presented by the following variables. Since all these variables are unsigned bytes with no units that are a function of time and height, the extra table columns have been removed for clearer presentation.

Classifications by type (8-bit unsigned integers)

aerosol_classification_direct <i>(aerosol classes derived without using a priori aerosol type map information)</i>	0 = ground 1 = none 2 -8 aerosol types 9 = don't know
aerosol_classification <i>(aerosol classes derived using a priori aerosol type map information)</i>	0 = ground 1 = none 2 -8 aerosol types 9 = don't know
Ice_classification	0 = ground 1 = none 2 = ice or snow (implicit assumption that observationally they are a continuum) 3 = Inconsistent (ice reported for web-bulb temperature >0 °C) 4 = stratospheric cloud (PSC-I non depolarizing) 5 = stratospheric cloud (PSC-II depolarizing) 9 = don't know
liquid_classification	0 = ground 1 = none 2 = warm liquid cloud (wet-bulb temperature > 0°C) 3 = Inconsistent (water reported for temperature < -40°C) 4 = supercooled 9 = don't know

<i>Class Probabilities (array of integers) Dimension (nz,n classes)</i>	
Classification probabilities_direct	<p>0-100 for each allowed lidar only class</p> <p>Allowed classes are:</p> <ol style="list-style-type: none"> 1. Surface 2. No target present (Clear air) 3. Water 4. Super Cooled Water 5. Ice 6. Aerosol type 1 7. Aerosol type 2 8. . 9. Etc <p>For any height bin, a negative entry present in each category means that no estimate is possible (i.e. lidar signal is completely attenuated)</p>
Classification probabilities <i>(aerosol classes derived using a priori aerosol type map information. Other classes are preserved for consistency)</i>	<p>0-100 for each allowed lidar only class</p> <p>Allowed classes are:</p> <ol style="list-style-type: none"> 1. Surface 2. No target present (Clear air) 3. Water 4. Super Cooled Water 5. Ice 6. Aerosol type 1 7. Aerosol type 2 8. . 9. Etc <p>For any height bin, a negative entry present in each category means that no estimate is possible (i.e. lidar signal is completely attenuated)</p>

5.4 Algorithm flow charts and Definition

5.4.1 Overall Algorithm Structure

The overall high-level structure of the main algorithm is shown in Figure 10. Here the Yellow trapezoids represent input or output data sets. Each of the main algorithm steps are label (A1, A2 etc..) and will be described in more detail in turn in the following sections.

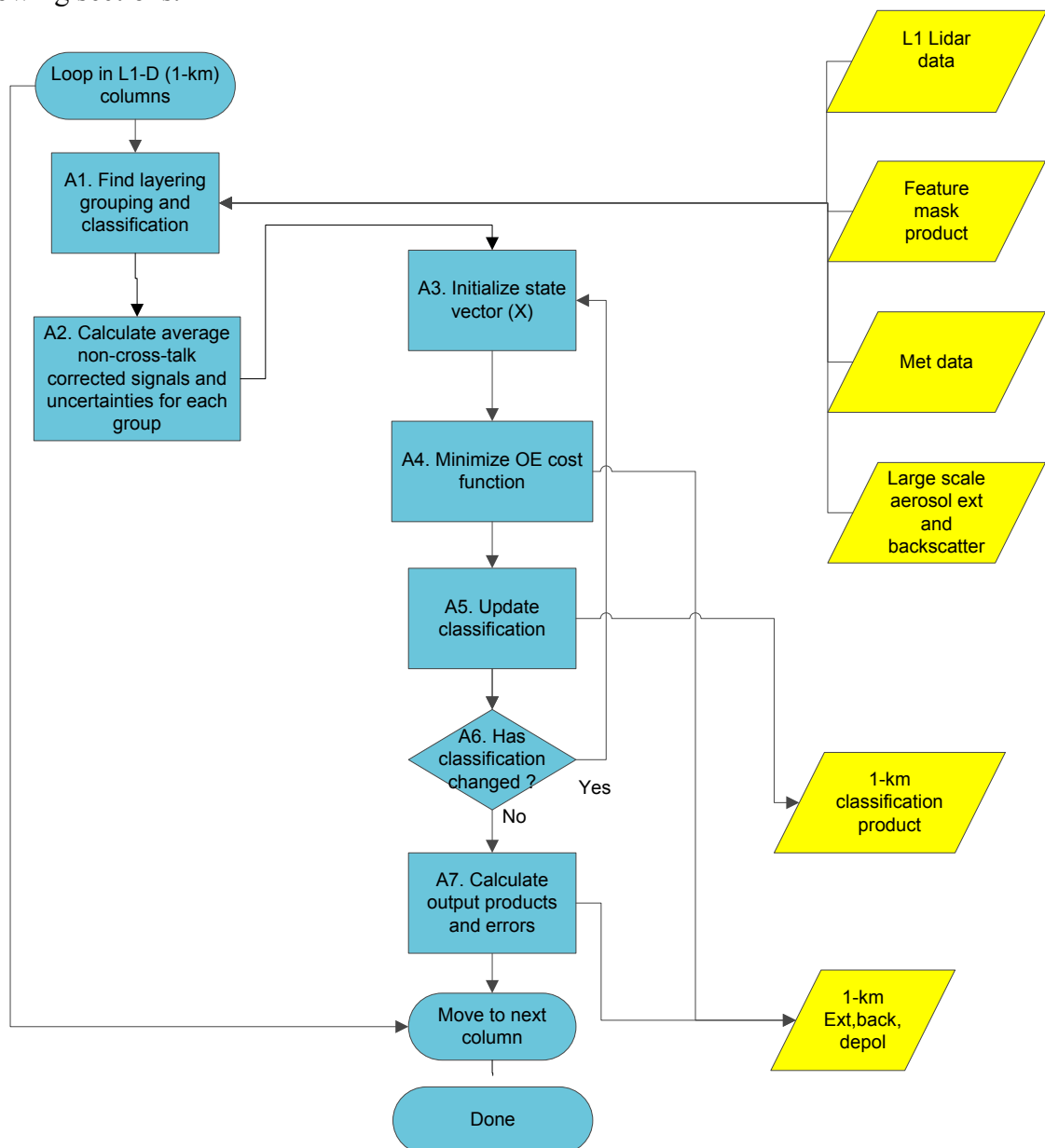


Figure 10: High-level structure of the main algorithm. Here the Yellow trapezoids represent input or output data sets.

5.4.2 Expanded View of A1: Find Layering, Grouping and Classification

Here an expanded view of the processes associated with step A1 of Figure 10 is presented.

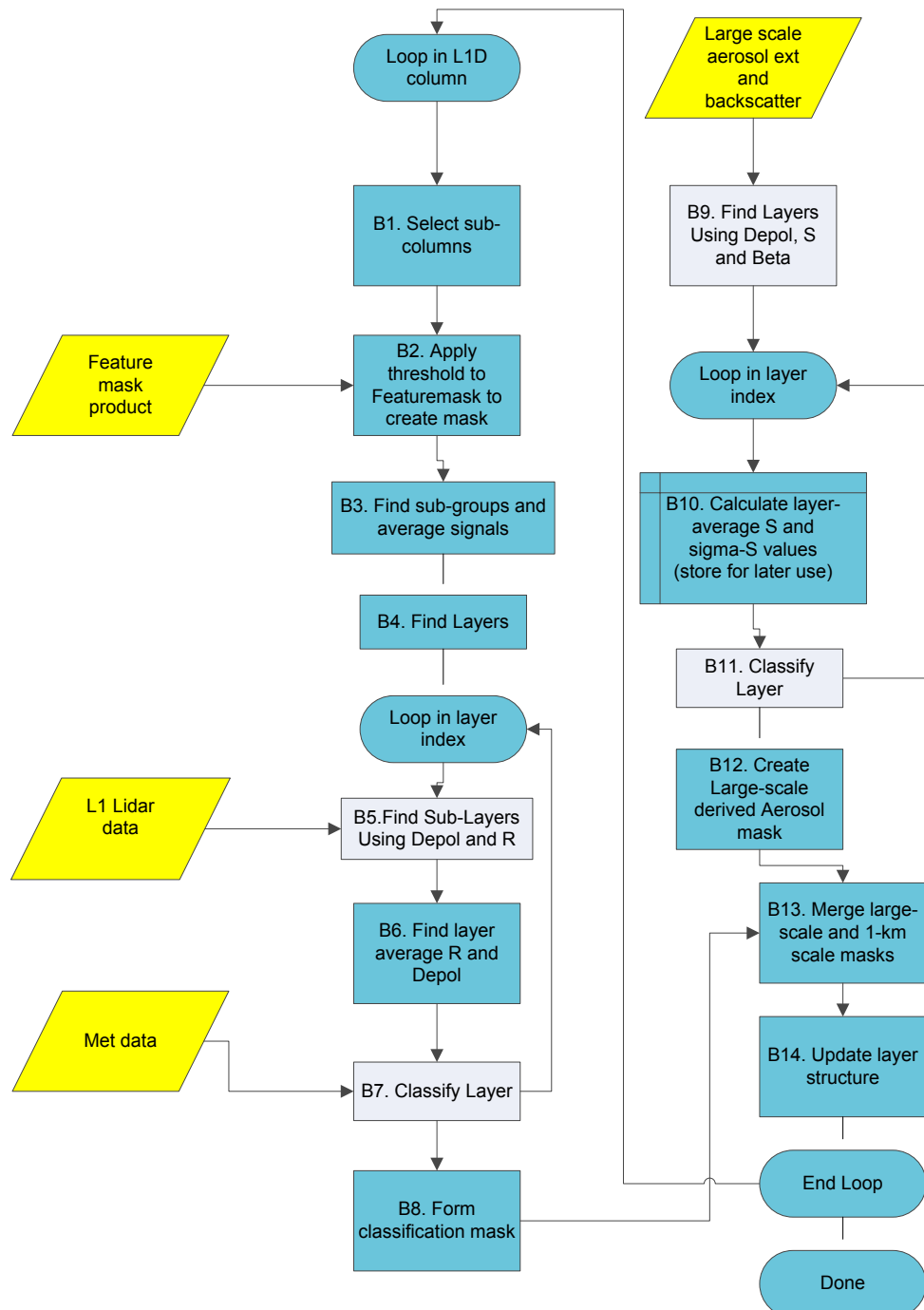


Figure 11: Schematic description of the steps involved in the layer, grouping and classification step (A1: Figure 10). Here the light-Grey-Blue boxes denote processes that are separately described in detail in [A-TC-ATBD].

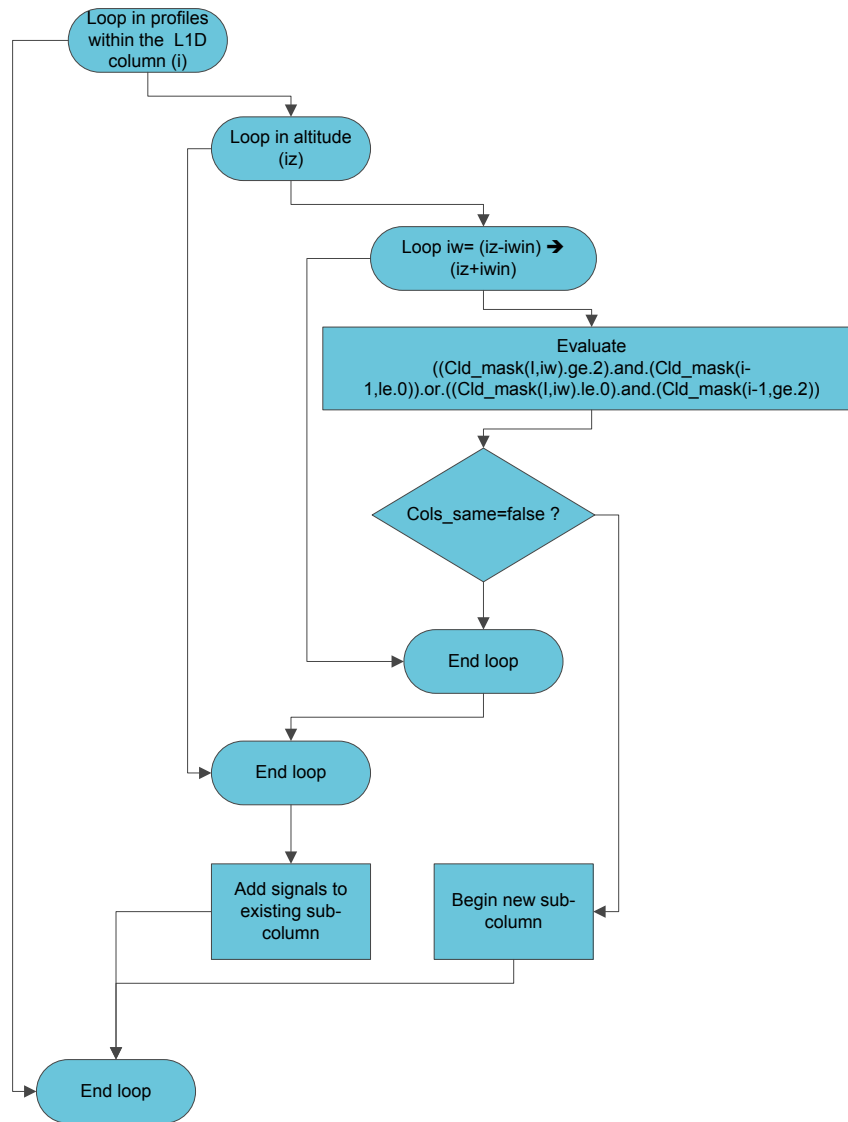


Figure 12. Expanded schematic of box B3 of Figure 11.

5.4.3 Expanded view of A4: Mimimize Optimal Estimation Cost function

The processes associated with the A4 process box in Figure 10 are shown in Figure 11.

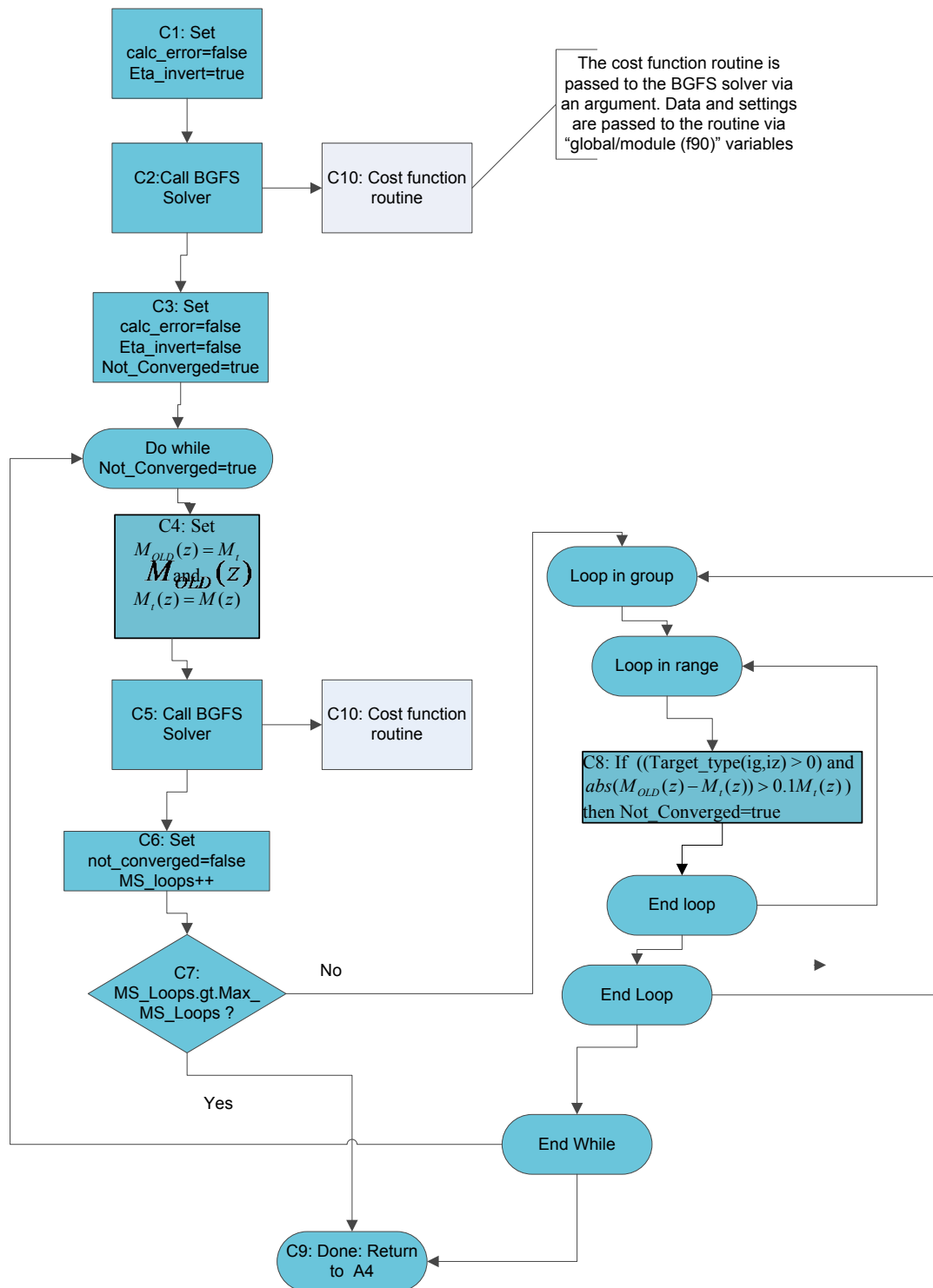


Figure 13: Expanded view of Box A4: Minimize Optimal estimation cost-function in Figure 10.

5.4.4 Expanded view of Box C10: Cost function routine

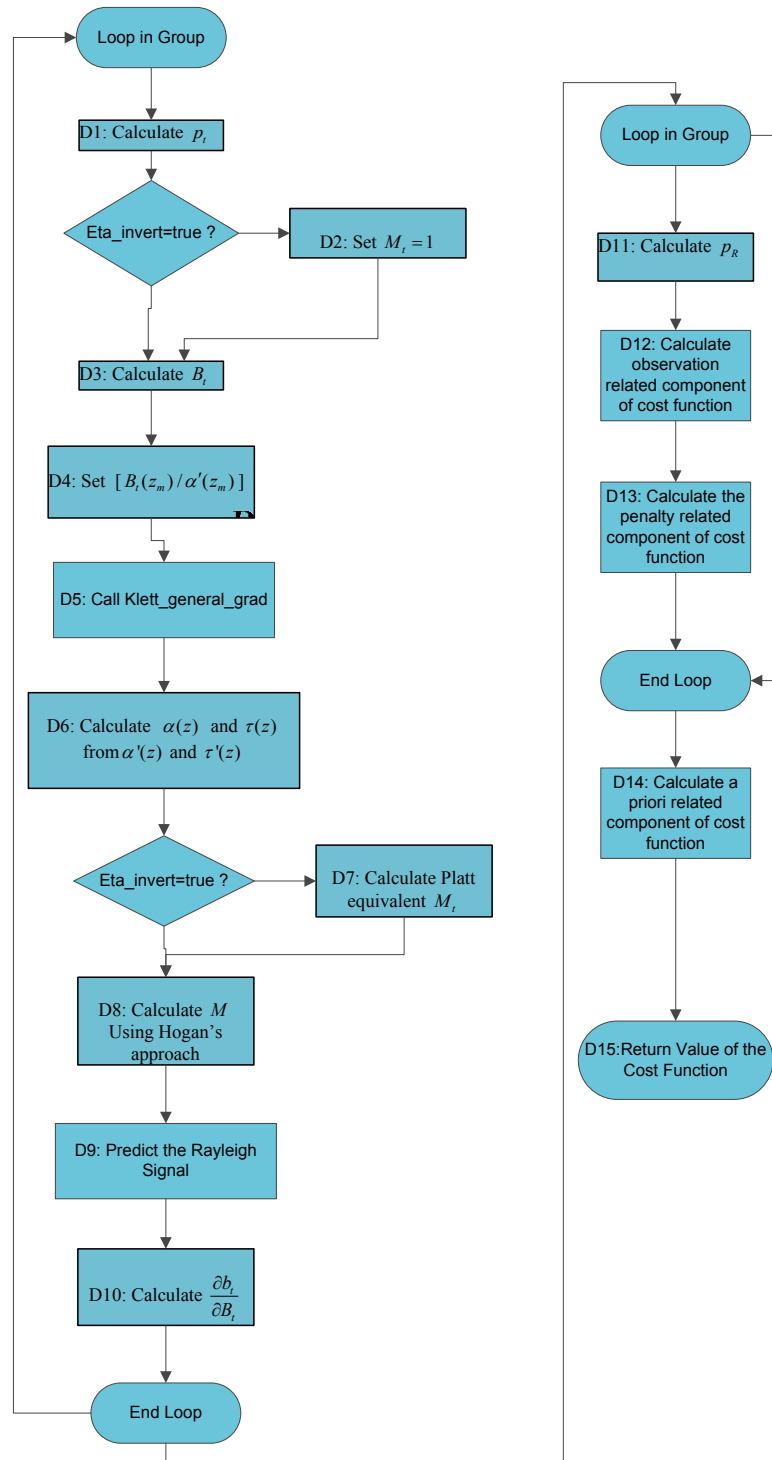


Figure 14. Expanded view of Box C10: Cost function routine in Figure 13.

5.4.5 Expanded view of Box D5: Call Klett_General_Grad

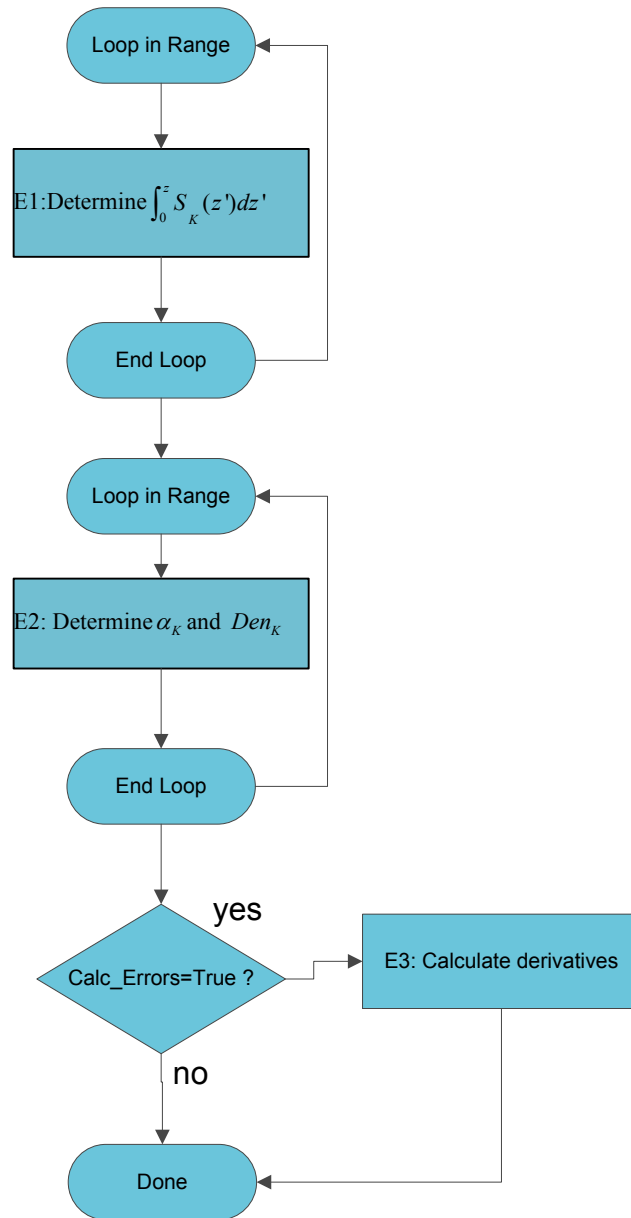


Figure 15. Expanded view of Box D5: Call Klett_General_Grad in Figure 14.

5.4.6 Expanded View of Box A7: Calculate Output Products and Errors

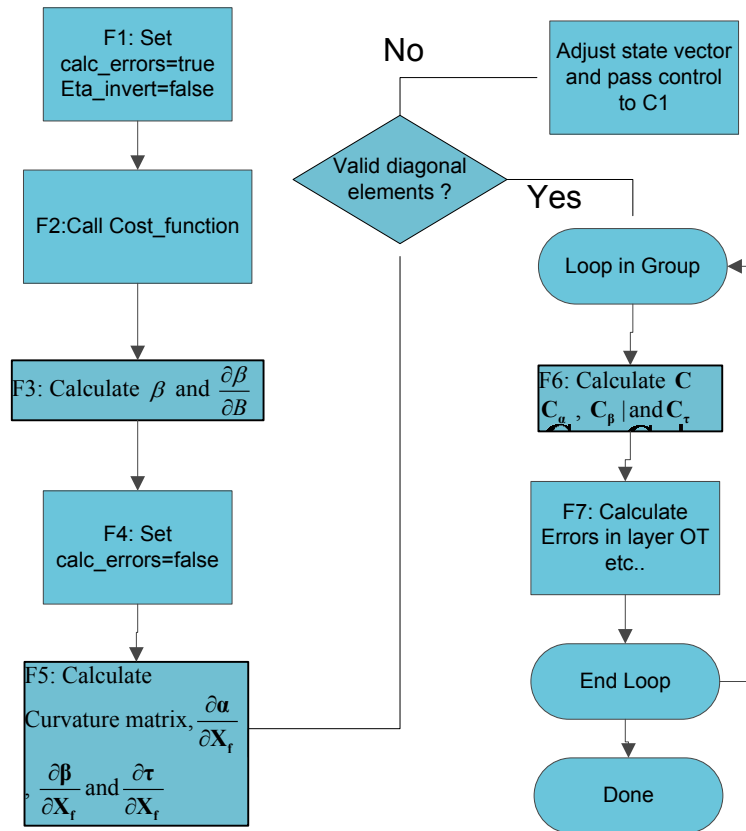


Figure 16: view of Box A7: Calculate Output Products and Errors in Figure 10.

5.5 Algorithm Definition

The overall high-level structure of the main algorithm is shown in Figure 10. Here the Yellow trapezoids represent input or output data sets. Each of the main algorithm steps are label (A1, A2 etc..) and will be described in more detail in turn in the following sections.

5.5.1 A1: Find Layering, Grouping and Classification

The sub-processes associated with the **A1** process box in Figure 10 are shown in Figure 11 in Section 5.4.2. An expanded presentation of the processes associated with step **A1** of Figure 10 is follows in the next subsection.

5.5.1.1 B1: Select sub-columns:

Here the indices corresponding to the L1 lidar profiles corresponding to the output L1D columns are found. In addition, the “translation” from the L1b parameters to the necessary information needed by the algorithm is conducted. Making use of Section 8.9.3 of [EADS-A-L1-ATBD] for our definition of the calibration and crosstalk parameters and their associated errors we find that

$$C_R = \hat{K}_{Ray}^0 \left(\frac{\tau_{Ray}(\theta_{nh})}{\tau_{Ray}(\theta_{Ref})} \right) \quad (3.38)$$

$$C_M = \frac{\hat{K}_{Mie}^0}{\hat{K}_p^{HSR}} \quad (3.39)$$

$$C_{cr} = \hat{K}_{Cro}^0 \quad (3.40)$$

$$\sigma_{C_M}^2 = C_M^2 \left[\left(\frac{errKmie}{\hat{K}_{Mie}^0} \right)^2 + errTpeak^2 \right] \quad (3.41)$$

$$\sigma_{C_R}^2 = C_R^2 \left[\left(\frac{errKray}{\hat{K}_{Ray}^0} \right)^2 + errTauR^2 \right] \quad (3.42)$$

$$\sigma_{C_{cr}}^2 = C_{Cr}^2 \left(\frac{errKcro}{\hat{K}_{Cro}^0} \right)^2 \quad (3.43)$$

$$X(z) = \chi_{Ref} + \delta_\chi(z) \quad (3.44)$$

$$\sigma_E = \sigma_\epsilon \quad (3.45)$$

$$E = \epsilon \quad (3.46)$$

$$\sigma_X = \sigma_\chi \quad (3.47)$$

For definitions of the various L1 quantities the reader is referred to **Table 1**.

The relationship between the cross-talk corrected and calibrated signal variables used in this algorithm and those read from the L1b ATLID data are given by

$$p_R^{co}(z) = RZ(z)^{-2} Ray_{inp} \quad (3.48)$$

$$p_t^{cr}(z) = RZ(z)^{-2} CRO_{inp} \quad (3.49)$$

and

$$p_M^{co}(z) = RZ(z)^{-2} MieCop_{inp} \quad (3.50)$$

At the time of this writing the reported science data errors (*ScDataErr*) contains both *noise* variance terms as well as terms best considered as *biases*. In this algorithm (and in most conceivable lidar retrieval algorithms) in order to generate useful error estimates the distinction between random and systematic errors must be taken into account. Thus we must estimate the random error component on the reported L1b backscatters. Accordingly, we have

$$\sigma_{p_R^{co}}^2 = \left(p_R^{co} \right)^2 \left(\left(\frac{ScDataErr_{Ray}}{Ray_{inp}} \right)^2 - \left(\frac{errKray}{\hat{K}_{Ray}^0} \right)^2 - errTpeak^2 \right) \quad (3.51)$$

$$\sigma_{p_M^{co}}^2 = \left(p_M^{co} \right)^2 \left(\left(\frac{ScDataErr_{Mie}}{MieCop_{inp}} \right)^2 - \left(\frac{errKmie}{\hat{K}_{Mie}^0} \right)^2 - errTauR^2 \right) \quad (3.52)$$

$$\sigma_{p_t^{cr}}^2 = \left(p_t^{cr} \right)^2 \left(\left(\frac{ScDataErr_{Cro}}{Cro_{inp}} \right)^2 - \left(\frac{errKcro}{\hat{K}_{Cro}^0} \right)^2 \right) \quad (3.53)$$

Again, for definitions of the various L1 quantities the reader is referred to **Table 1**.

5.5.1.2 B2: Apply threshold to Feature Mask data

1. FeatureMask data for the range of columns identified in B1 are read in.
2. $(FeatureMask(id,j) \geq FM_Thres) \rightarrow Cld_Mask(i,j)=1$
3. $(FeatureMask(id,j) \geq FM_Thres_Strong) \rightarrow Cld_Mask(i,j)=2$

5.5.1.3 B3: Find sub-groups, average signals (see also Section 3.3.4 Horizontal Signal binning)

This process groups and averages 'like' profiles within the L1D column being processed. In order that the process not be sensitive to "noise" that may be present within the *FeatureMask* profiles, only differences in "strong" features are considered and a vertical buffer of *iwin* resolution steps is taken into account when deciding the profile grouping. The schematic depiction of this process is given in Figure 12.

5.5.1.4 B4: Find Layers

The layer boundaries are found by looping over the *Cld_Mask* variable. A target is considered present at a given range if any entry within in the L1D horizontal resolution volume is equal to 1 or 2. Vertical layers are determined by the occurrence of gaps between continuous vertical regions where targets are present.

5.5.1.5 B5: Find Sub-Layers using R and Depol

The vertical layer structure found in step **B4** is based solely on the basis of the presence of a target of any type. Thus, it is necessary to check if the layers seem to be composed of a single-target type or if it is necessary to create additional layers by splitting of the layers determined in step **B4**.

1. For each layer the profile of Backscatter Ratio (*R*) and the corresponding error estimate are computed.

The backscatter ratio used for this processing step is found directly from the ratio of the sum of the Mie channel and the Cross-polar channel to the Rayleigh channel. i.e.

$$R = \left(\frac{\beta_M + \beta_{Ray}}{\beta_{Ray}} \right) \approx \frac{\langle p_M^{co} \rangle + \langle p_t^{cr} \rangle + \langle p_R^{co} \rangle}{\langle p_R^{co} \rangle} \quad (5.1)$$

where we have assumed that the cross-polar Rayleigh return may be neglected and that the effects of Multiple-scattering are the same for both the Rayleigh and Mie Channel returns. Here the braces denote horizontal averaging over the L1D resolution volume but only where $Cld_Mask(i,j) \geq 1$.

The corresponding variance in the Backscatter Ratio is given by

$$\sigma_R = \left[\frac{(R-1)^2}{\langle p_R^{co} \rangle^2} \left(\sigma_{\langle p_R^{co} \rangle}^2 + \left(\frac{\langle p_R^{co} \rangle}{C_R} \right)^2 \sigma_{C_R}^2 \right) + \left(\frac{1}{\langle p_R^{co} \rangle^2} \right) \left(\sigma_{\langle p_M^{co} \rangle}^2 + \left(\frac{\langle p_M^{co} \rangle}{C_M} \right)^2 \sigma_{C_M}^2 \right) + \left(\frac{1}{\langle p_R^{co} \rangle^2} \right) \left(\sigma_{\langle p_t^{cr} \rangle}^2 + \left(\frac{\langle p_t^{cr} \rangle}{C_{Cr}} \right)^2 \sigma_{C_{Cr}}^2} \right) \right]^{1/2} \quad (5.2)$$

where, for simplicity, we have assumed the errors in each of the respective signals is uncorrelated (i.e. correlations between the Mie and Rayleigh signals due to the presence of cross-talk are neglected here) and

$$\sigma_{\langle p_M^{co} \rangle}^2 = \frac{\sum_{\substack{\text{where} \\ \text{Cld-mask} \geq 1}} \sigma_{p_M^{co}}^2(i)}{\sum_{\substack{\text{where} \\ \text{Cld-mask} \geq 1}} 1}. \quad (5.3)$$

Similar expressions hold for the $\sigma_{\langle p_t^{cr} \rangle}^2$ and $\sigma_{\langle p_R^{co} \rangle}^2$.

2. The Depolarization Ratio (δ) profile is estimated by neglecting the small contribution of Rayleigh scattering to the cross-polar channel so that

$$\delta \approx \left(\frac{\langle p_t^{cr} \rangle}{\langle p_M^{co} \rangle} \right) \quad (5.4)$$

The corresponding variance is given by

$$\sigma_\delta \approx \delta \left[\left(\frac{1}{\langle p_M^{co} \rangle} \right)^2 \left(\sigma_{\langle p_M^{co} \rangle}^2 + \left(\frac{\langle p_M^{co} \rangle \sigma_{C_M}}{C_M} \right)^2 \right) + \left(\frac{1}{\langle p_t^{cr} \rangle} \right)^2 \left(\sigma_{\langle p_t^{cr} \rangle}^2 + \left(\frac{\langle p_t^{cr} \rangle \sigma_{C_{Cr}}}{C_{Cr}} \right)^2 \right) \right]^{1/2} \quad (5.5)$$

3. For each layer identified in step **B4** the corresponding profiles of R and δ and their respective error estimates are fed into the *Significant-Layer identification routine*. This procedure identifies statistically significant transitions within the profiles. If (sub-)layers are identified within the layers identified in step **B4** the layering structure is adjusted to accommodate the identified sub-layers by appropriately splitting the layers. The *Significant-Layer identification* procedure is not described further here. A detailed description may be found inside [A-TC-ATBD].

5.5.1.6 B6: Find layer average R and δ

Here, for each vertical layer identified in step **B5**, the layer average values of backscatter ratio $\langle R \rangle_{lay}$ and depolarization are found $\langle \delta \rangle_{lay}$ by appropriate averaging of the values already computed in step B5. Error estimates are also computed via standard quadratic summation of the errors and division by the square-root of the number of samples.

5.5.1.7 B7: Classification of Layers

Each layer is assigned a classification index. This is accomplished by calling the *Target classification* procedure supplying the layer-averaged backscatter and depolarization ratio. The main function of this routine is to classify each layer

identified in step **B6** as being Ice-Cloud, Water-Cloud (including supercooled), PSC or aerosol.

The *Target classification* procedure is not described further in this document but is described in detail within [A-TC-ATBD].

5.5.1.8 B8: Form classification mask

Here the classification information in **B7** is 'expanded' to form a classification mask at the lidar native vertical resolution. This step is necessary in preparation to the merging of the layer information found in steps **B4-B7** with the layer information to come from steps **B9-B12**.

5.5.1.9 B9: Find Layers using Depol, S, and R

This step is similar to step **B5**. However, the values of S , δ and R are derived from the *large-scale aerosol backscatter, extinction and depolarization ratio* algorithm output. The respective profiles (along with their error estimate profiles) corresponding to the L1D column being processed are fed into the same *Significant-Layer identification routine* used in step **B5**.

5.5.1.10 B10: Calculate layer average S and σ_s values.

For each of the layers identified in step **B9** the layer average values of S_a and σ_{s_a} are calculated as described previously in Section 3.3.6. These values are stored for later use in setting up the state vector for optimal estimation inversion.

5.5.1.11 B11: Classification of aerosol layers

This step involves calling the *aerosol typing algorithm* which is described in [A-TC-ATBD] in order to assign an aerosol index to each layer identified in step **B10**.

5.5.1.12 B12: Form aerosol type mask.

Here, similar to step **B8**, the aerosol layer classification information is expanded to form an aerosol type mask at the lidar native resolution.

5.5.1.13 B13: Merge large-scale derived and 1-km scale Masks.

At this step the 1-D masks from steps **B8** and **B12** are merged into a single mask. The merging is accomplished by starting with the 1-km cloud/aerosol mask and then imposing the aerosol mask for but only for altitudes where the 1-km mask does not indicate the presence of clouds. Any aerosols altitudes present in the 1-km mask but not present in the large scale aerosol type mask are assigned the same aerosol type as the closest in altitude aerosol mask entry.

5.5.1.14 B14: Update layer structure

Here the layering structure for the L1D column being processed is re-derived using the output type mask from step **B13**. Changes in the assigned type with altitude are used to indicate boundaries between layers.

5.5.2 A2: Calculate Average Non-crosstalk Corrected Signals and Uncertainties for each Group

Here average values of $p_{o.M}^{co}(z)$ and $p_{o.R}^{co}(z)$ are calculated using the average L1 cross-talk corrected signals calculated in Step B3. The calculations follow Section 3.3.3.

5.5.3 A3: Initialize State Vector

Using the target classification information and, for aerosol layers, the information derived from the large-scale aerosol product the state vector is initialized to the first guess values. The a priori state vector and the associated variance matrix are also initialized. It should be noted that the first-guess values are not necessarily the same as the a priori values.

5.5.4 A4: Minimize Optimal Estimation Cost function

A simplified description of the sub-steps associated with A4 have been given in Figure 2 and Figure 5. Here a more detailed description is given. The sub-steps associated with the A4 process box in Figure 10 are shown in Figure 11 and are described in the following subsections.

5.5.4.1 C1: Set *calc_errors=false, Eta_invert=true*

These settings are passed using global storage to the Cost Function Routine (C10). These settings tell the routine not to calculate derivatives needed for detailed error calculations and to account for multiple-scattering effects in the inversion set using Platt's method.

5.5.4.2 C2: Call *BGFS solver*

The minimization solver is called in order to minimize the cost function. No derivatives are calculated and Platt's MS approach is used to calculate M_t .

5.5.4.3 C3: Set *calc_error=false etc.*

The global variable **Eta_invert** is set to **False** so that subsequent calls to the cost function routine will use Hogan's multiple scattering model. The **Not_Converged** variable is set to **False**.

5.5.4.4 C4: Set $M_{OLD}(z) = M_t$ and $M_t(z) = M(z)$

The old MS correction is stored and the total MS factor is set to $M(z)$ which is always calculated using Hogan's model even when **Eta_invert=true**.

5.5.4.5 C5: Call *BGFS solver*

The minimization solver is called in order to minimize the cost function. No

derivatives are calculated and Hogans's MS approach is used to calculate M_t .

5.5.4.6 C6: Set not_converged=false and MS_loops++

The MS_loops counter is incremented and the **not_converged** variable is set to **false**.

5.5.4.7 C7: MS_loops gt. Max_MS_loops

If the number of while loop passes exceeds the maximum allowed then the while loop is exited.

5.5.4.8 C8: If ((Target_type(ig,iz) etc..

This step checks for convergence in the Multiple-scattering correction factor. If convergence is not found then **not_converged=true**

5.5.4.9 C9: Done

The procedure is finished. Control is passed back to step **A5**.

5.5.4.10 C10: Cost function routine

This routine is perhaps the key component of the procedure described in this ATBD. Along with the calculation of the cost function itself (Eqn.(3.24)) several other important calculation are carried out within this procedure. The processes associated with **C10** are depicted schematically in Figure 14 and Figure 15 and are described in the following subsections.

5.5.4.10.1 D1: Calculate p_t^f

Here p_t^f calculated according to Eqn. (3.22)

5.5.4.10.2 D2: Set $M_t = 1$

If Platt's MS approach is to be used then the value of M_t is initialized to 1.

5.5.4.10.3 D3: Calculate B_t

Here B_t is calculated according to Eqn.(3.4)

5.5.4.10.4 D4: Set $B_t(z_m)/\alpha'(z_m)$

The boundary value to be used in the Klett-type inversion is set at this point. The boundary range (z_m) is chosen to be a clear-sky altitude above the highest cloud detection. In this case, $\alpha(z_m)$ is zero and $S(z_m) = 1$ so that following Eqn.(3.11)

$$\left(\frac{B_t}{\alpha'} \right)_{z_m} = \exp \left[-2 \int_{z_{lid}}^z \beta_R(z') dr' \right] \quad (5.6)$$

5.5.4.10.5 D5: Call Klett_general_grad

Here a call is made to the routine that implements a “Klett-like” inversion following Eqn.(3.9). The solver is generic and the transformation between, for example, α' and α must be accomplished externally. The Klett routine is described in the following subsections.

5.5.4.10.5.1 E1: Determine Denominator

The integral in in the denominator in Eqn. (3.9) is calculated and stored.

5.5.4.10.5.2 E2: Determine α' and Den

α' is found according to (3.9) and Den is found following Eqn (3.35).

5.5.4.10.5.3 E3: Calculate derivatives

Various derivatives that will be used later in error calculations are analytically computed.

$$\begin{aligned}\frac{\partial \alpha'_i}{\partial B_{M,j}} &= \text{Sign}(\alpha_i) \alpha_i'^2 \Delta r_j (B_{M,j})^{-2} & j > i \\ &= \text{Sign}(\alpha_i) \alpha_i'^2 \Delta r_i (B_{M,i})^{-2} + \frac{\alpha'_i}{B_{M,i}} & j = i \\ &= 0 & j < i\end{aligned}\quad (5.7)$$

where Δr_j is the width of the j th line-of-sight range bin.

5.5.4.10.6 D6: Calculate $\alpha(z)$ and $\tau(z)$ from $\alpha'(z)$ and $\tau'(z)$

Eqns. (3.6) and (3.8) are used to transform between $\alpha'(z)$, $\tau'(z)$ and $\alpha(z)$, $\tau(z)$

5.5.4.10.7 D7: Calculate Platt equivalent M_i

If a Platt-type MS approach is desired then the effective M_i profile is calculated following Eqn.(3.8).

5.5.4.10.8 D8: Calculate M using Hogan’s approach.

This step is accomplished by a call to a modified version of the routine **multiscatter_qsa** the routine has been modified to return M instead of absolute signals.

5.5.4.10.9 D9: Calculate the Predicted Rayleigh Signal.

The values of the predicted calibrated and cross-talk corrected Rayleigh Signal are

generated according to Eqn. (3.12). These values serve as the forward model vector (the y_{i_g} values in Eqn. (3.24)). It was found that the convergence properties were improved if, in the calculation of the optical thickness used in Eqn. (3.12), values of $\alpha(z)$ were limited to values greater than about $-1.0e-4$ 1/m (i.e. too negative values of the extinction are clipped).

5.5.4.10.10 D10: Calculate $\frac{\partial B_t}{\partial b_t}$

Here $\frac{\partial B_t}{\partial b_t}$ is calculated and stored. These partial derivatives will be used at other steps in the algorithm, particularly in steps involving error calculations. Using Eqn.(3.4) it follows that

$$\frac{\partial B_t}{\partial b_t}(z) = \exp \left[-2 \int_{z_{lid}}^z S(z') \beta_R(z') dr' \right] S(z) \quad (5.8)$$

5.5.4.10.11 D11: Calculate p_R^f

Here the cross-talk corrected Rayleigh scattering signals are constructed following Eqn. (3.23) account for the adjust factors.

5.5.4.10.12 D12: Calculate observation related component of cost function

Here the observational part of the cost function (Left-hand side of Eqn. (3.24)) is calculated and stored for diagnostic use.

5.5.4.10.13 D13: Calculate the penalty related component of cost function

Here the a priori part of the cost function (Eqn.(3.35)) is calculated and stored for diagnostic use.

5.5.4.10.14 D14: Calculate a priori related component of cost function

Here the a priori part of the cost function (Right-hand side of Eqn. (3.24)) is calculated and stored for diagnostic use.

5.5.4.10.15 D15: Return Value of the Cost Function

The value of the total cost function is stored and passed back to the calling routine.

5.5.5 A5: Update Classification

Here the classification step (described in step **B7** in Section 5.4.2 and called via step

A1) is called again. However with different inputs. In particular in this step, layer average values of β and α produced by the OE procedure are used as input to the classification routine.

5.5.6 A6: Has Classification Changed ?

If the the resulting updated classification mask produced by step **A5** is not consistent with the earlier mask used in the inversion process, then the mask is updated and another inversion is conducted. This process can loop only for a set number of times.

5.5.7 A7: Calculate Output Products and Errors

Here the various output products are calculated as well as their associated errors. This includes are calculation of the the retrieved state vector covariance matrix.

5.5.7.1 F1: Set *calc_errors=true*. *Eta_invert=false*

Set flag variables so that the call to the cost function will calculate M_t using Hogan's model and derivatives will be calculated.

5.5.7.2 F2: Call Cost function

The cost function is called

5.5.7.3 F3: Calculate β and $\frac{\partial\beta}{\partial B}$

The backscatter profile is calculated according to

$$\beta(z) = \alpha(z)S^{-1}(z) \quad (5.9)$$

and

$$\frac{\partial\beta(z)}{\partial B_t(z)} = \frac{\partial\alpha(z)}{\partial B_t(z)}S^{-1}(z) \quad (5.10)$$

5.5.7.4 F4: Set *calc_errors=false*.

Turn off derivative calculations in folowwing cost function calls.

5.5.7.5 F5: Calculate Curvature Matrix etc..

The curvature matrix associate with the state-vector is calculated numerically

$$\left[\frac{\partial^2 \chi^2}{\partial x_i^f \partial x_j^f} \right] \approx \frac{(\chi^2(X^f - \Delta X_i^f) + \chi^2(X^f + \Delta X_i^f) - 2\chi^2(X^f))}{2|\Delta X_i^f|^2} \quad (5.11)$$

in the case of $i = j$ and

$$\frac{(\chi^2(X_f + \Delta X_i + \Delta X_j) - \chi^2(X_f + \Delta X_i - \Delta X_j) - \chi^2(X_f - \Delta X_i + \Delta X_j) + \chi^2(X_f - \Delta X_i - \Delta X_j))}{4|\Delta X_i||\Delta X_j|} \quad (5.12)$$

otherwise, where ΔX_i^f and ΔX_j^f are scaled unit vectors.

If negative diagonal elements are detected this means that either $(X^f + \Delta X_i^f)$ or $(X^f - \Delta X_i^f)$ are better approximations to the minimum. This likely signifies spurious convergence. In this case the state-vector is updated to either $(X^f + \Delta X_i^f)$ or $(X^f - \Delta X_i^f)$ and control is passed back to **Step C1**.

In addition, at this step

$\left(\frac{\partial \alpha(z)}{\partial X} \right)$, $\left(\frac{\partial \alpha(z)}{\partial X} \right)$ and $\left(\frac{\partial \tau(z)}{\partial X} \right)$ are calculated numerically using a simple centred difference technique.

5.5.7.6 F6: Calculate covariance Matrices

The state vector error covariance matrix is calculated by inverting the curvature matrix (see Eqn. (3.37)).

In order to calculate the extinction covariance matrix the following steps are performed:

1. The extended covariance matrix is constructed defined such that

$$\begin{aligned} [C_e]_{i,j} &= [C]_{i,j} \quad i, j \leq np \\ &= \sigma_{B_i, i-np}^2 \quad i = j, i, j > np \end{aligned} \quad (5.13)$$

where np is the dimension of \mathbf{X} .

2. The appropriate extinction Jacobian is formed. i.e

$$\begin{aligned}
 [J^\alpha]_{i,j} &= \frac{\partial \alpha_i}{\partial X_j} \\
 &\quad \frac{\partial \alpha_i}{\partial B_{t,j-np}} \\
 i, j &\leq np \\
 i = j, i, j &> np
 \end{aligned} \tag{5.14}$$

3. The extinction covariance is formed according to standard practice, i.e.

$$C_a = J_a C J_a^t \tag{5.15}$$

Similar steps are carried out for the backscatter and the optical depth.

5.5.7.7 F7: Calculate Layer integrated quantities and errors

Layer integrated values of extinction, backscatter, attenuated backscatter and depolarization are found by simple summation according to the layer structure. For the attenuated backscatter and depolarization ratio which are uncorrelated the error estimates are computed by quadratic summation of the appropriate errors. In the case of the extinction and backscatter the covariance information computed in step F6 is used, for example, if

$$OT = \sum_{i=1}^{z2} \alpha(z) \Delta z(z_i) \tag{5.16}$$

then

$$\sigma_{OT}^2 = \sum_{i=1}^{z2} \sigma_\alpha^2(z) \Delta z_i + \sum_{i=1}^{z2} \sum_{j=1}^{z2} [C_\alpha]_{i,j} \Delta z_j \Delta z_i \Big|_{i \neq j} \tag{5.17}$$

The same general procedure is used for the integrated backscatter.

6 Algorithm performance, sensitivity studies, limitations

A prototype algorithm has been coded in f90 and integrated into the ECSIM environment. Various scenes ranging from simple idealized cases to scenes based on actual airborne HSRL measurements have been used to test the algorithm.

6.1 Simple 1-D Cirrus Cases: a priori S sensitivity

In order to judge the sensitivity of the algorithm described in this document. As a first step, a number of simple single layer cirrus cases were constructed using ECSIM using the latest estimates of the lidar parameters (Jan 2011). These cases are listed below

CASE	OT	S	S_a	$\sigma_{S_a^f}$	R_a	Ra_a	$\sigma_{Ra_a^f}$
1a	1	20.8	20	2	42.7	50	0.5
1b	1	20.8	10	2	42.7	50	0.5
1c	1	20.8	40	2	42.7	50	0.5
2a	2	20.8	20	2	42.7	50	0.5
2b	2	20.8	10	2	42.7	50	0.5
2c	2	20.8	40	2	42.7	50	0.5

Table 5: Cirrus cases characteristics

Results from the simulations for Case-1 are shown in Figure 17. Here the horizontal resolution corresponds to 1-km. Here the first-guess S value is the same as the a priori value. For Case-1a, the optimal extinction profile is very close (but not identical) to the first guess profile. For cases 1b and 1c, the factor of 2 error in the first-guess S value actually causes the first-guess extinction profile calculation to become divergent. In particular, in Case-1b ($S_a=10$) values strongly tending to zero with increasing cloud penetration while in Case-1c ($S_a=40$) the first guess extinction profile tends to infinity. In spite of the divergent first-guess extinction profiles in both Cases 1b and 1c the retrieved optimal profiles closely resemble the Case 1a retrieved profile. It can be further be seen that the optical thickness of the cloud is well retrieved in all cases. This indicates that there is real information contained in the signals at the scale considered here. The same general picture holds for Case 2 (shown in Figure 18). However, here the errors in both the retrieved extinction and OD become very large at cloud bottom. This is due to the fact that, even with the reduced effective transmission caused by multiple scattering, that the optical thickness of this cloud is such that the lidar signals in the lowermost sections of this cloud have a SNR well below one (i.e. the Rayleigh signal below cloud base is statistically practically zero and thus contains very little information).

CASE	S	σ_S	R_a	σ_{R_a}
1a	21.93	1.74	49.01	26.24
1b	25.60	4.39	45.79	18.67
1c	25.97	1.11	50.47	27.72
2a	19.41	1.19	49.55	29.68
2b	19.32	2.19	52.74	29.43
2c	22.17	0.62	53.36	29.70

Table 6: Extinction-to-backscatter ratios and effective area weighed radii retrieved for the different cases along with their error estimates. Values of $S = 20.8$ Sr $R_a = 42.7$ microns were used in the forward model simulations.

The R_a and S elements of the retrieved state-vector for cases 1 and 2 are shown in Table 6 along with their error estimated derived from the appropriate diagonal element of the state-vector covariance matrix. Here it can be seen that in all cases that S is retrieved with reasonable accuracy and with a precision significantly greater than the corresponding a priori specification (here a factor of 2). However, for with respect to R_a this is not the case. In particular, it can be seen that the estimated standard deviation of the retrieved values is very close to the a priori uncertainty. This indicates that there is little size information contained in the measurements for the range of conditions used here. This, in fact, is expected on the basis of earlier work [cite final report, MS comparison with Hogan section] where it was found that for this range of optical depths and (> 25 micron) particle sizes that the MS was not sensitive to particle size. However, for smaller particle sizes we do expect sensitivity. This issues is not further explored in this ATBD but is recommended for further study.

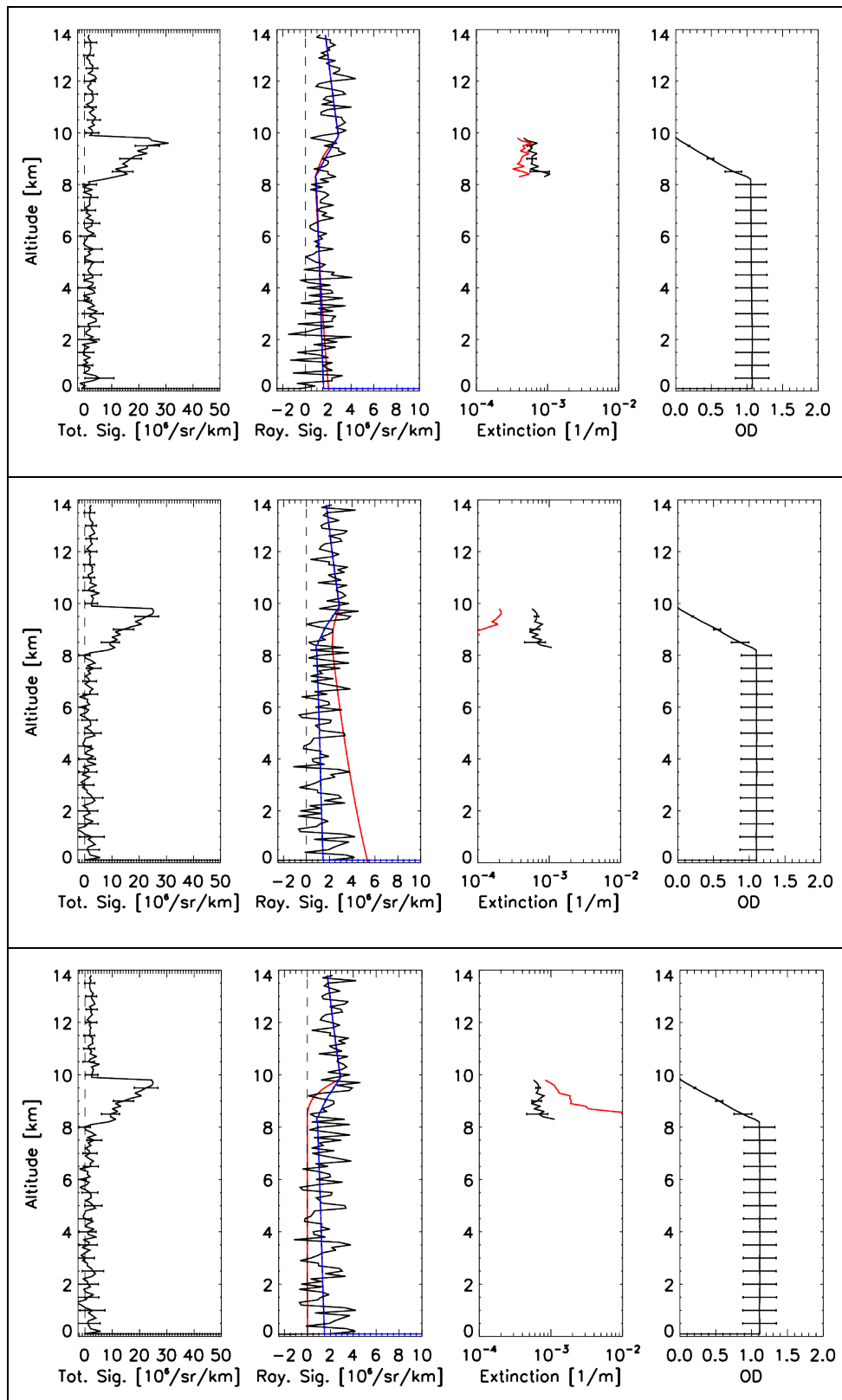


Figure 17: Inversion results for Case 1a (Top), 1b, (Middle) and 1c (Bottom). In the 3rd column the Red lines show the first guess extinction retrieval and the Black-line the best estimate profile. In the 2nd column the Red lines shows the first-guess predicted Rayleigh signal while the Blue-line shows the best estimate profile. The 4th column shows the cloud optical depth.

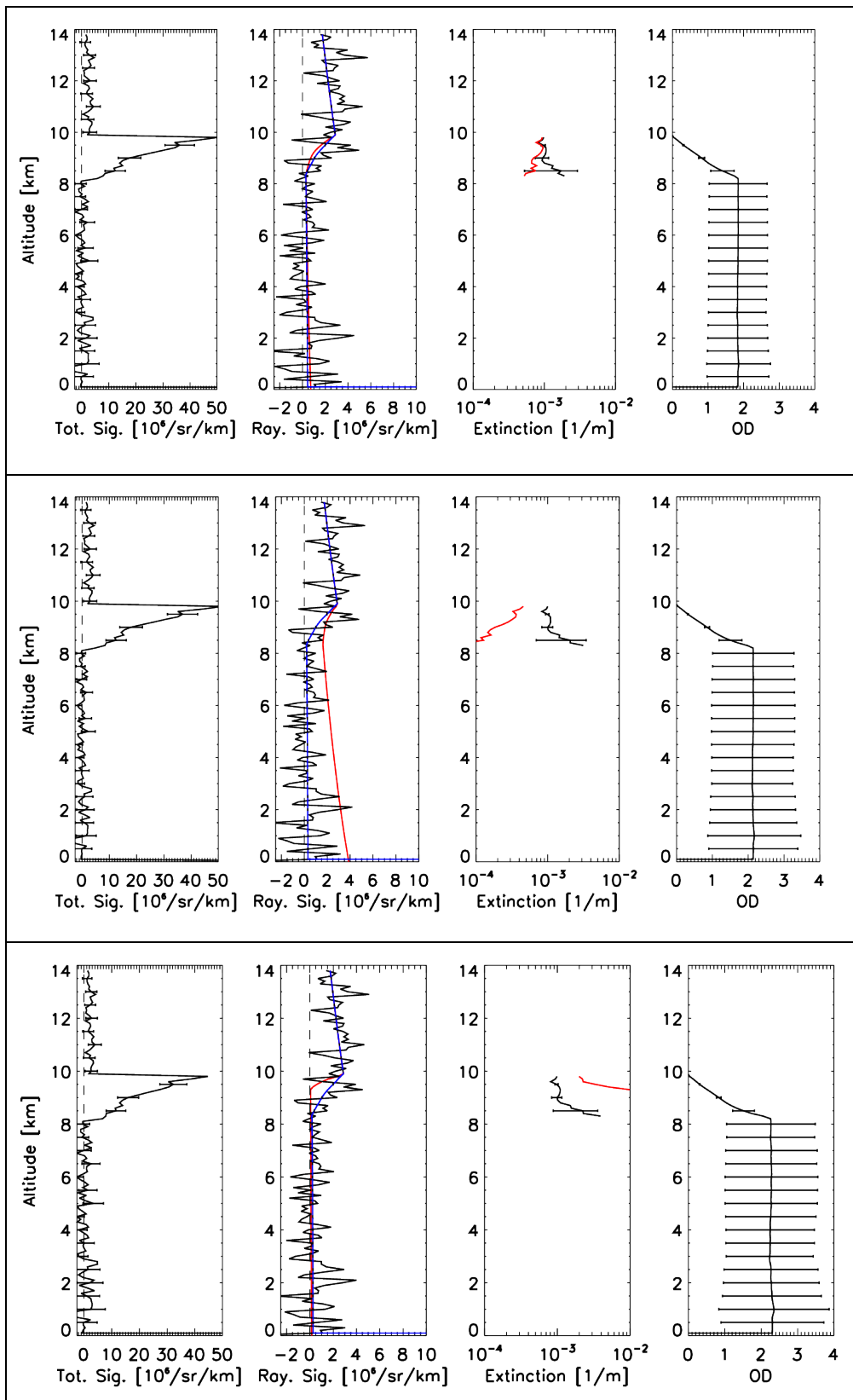


Figure 18: Inversion results for Case 2a (Top), 2b, (Middle) and 2c (Bottom). In the 3rd column the Red lines show the first guess extinction retrieval and the Black-line the best estimate profile. In the 2nd column the Red lines shows the first-guess predicted Rayleigh signal while the Blue-line shows the best estimate profile. The 4th column shows the cloud optical depth.

6.2 Simple 1-D Cirrus Cases: a priori Cross-Talk coefficients sensitivity

Here the effect of errors in the specification of the cross-talk coefficients are presented. As an example, a comparison of the results achieved using the Case-1a scenario but intentionally incorrectly under – (Case 3a) and over-specifying (Case 3b) the E (Mie→Rayleigh) coefficient by 50% (See Table 7) is shown in Figure 19 and the corresponding retrieved cross talk factors and extinction-to-backscatter ratios are listed in Table 8. It can be seen that reasonable results are obtained for both cases, in spite of the fact that the misspecification is quite large. It can also be seen that in the (under-estimation case) Case-3a that the retrieved C_x value is very close to the a priori but in the (over-estimation) Case-3b that the correct value of C_x is recovered. Consistent with this observation is the fact that the retrieved profile of the Rayleigh Signal for Case-3a is very close to the first guess profile while for Case-3b there is a notable difference. Similar results were obtained using variations of Case-2. At this point, the reasons for this asymmetric behaviour are unclear and will require further investigation.

CASE	$f_{K_{M_a}}, f_{X_a}, f_{K_{R_a}}$	$\sigma_{f_{K_{M_a}}}, \sigma_{f_{X_a}}, \sigma_{f_{K_{R_a}}}$	f_E	σ_{f_X}
3a	1	0.1	0.5	0.2
3b	1	0.1	1.5	0.2

Table 7: C_x sensitivity cases.

CASE	f_{K_M}	$\sigma_{f_{K_M}}$	f_X	σ_{f_X}	f_E	$\sigma_{f_{C_M}}$	f_{C_R}	$\sigma_{f_{K_R}}$	S	σ_S
3a	0.96	0.09	0.99	0.1	0.51	0.18	1.0	0.08	20.1	1.55
3b	1.1	0.1	1.0	0.1	1.17	0.2	1.0	0.08	23.7	2.1

Table 8: Results for Cases 3a and 3b.

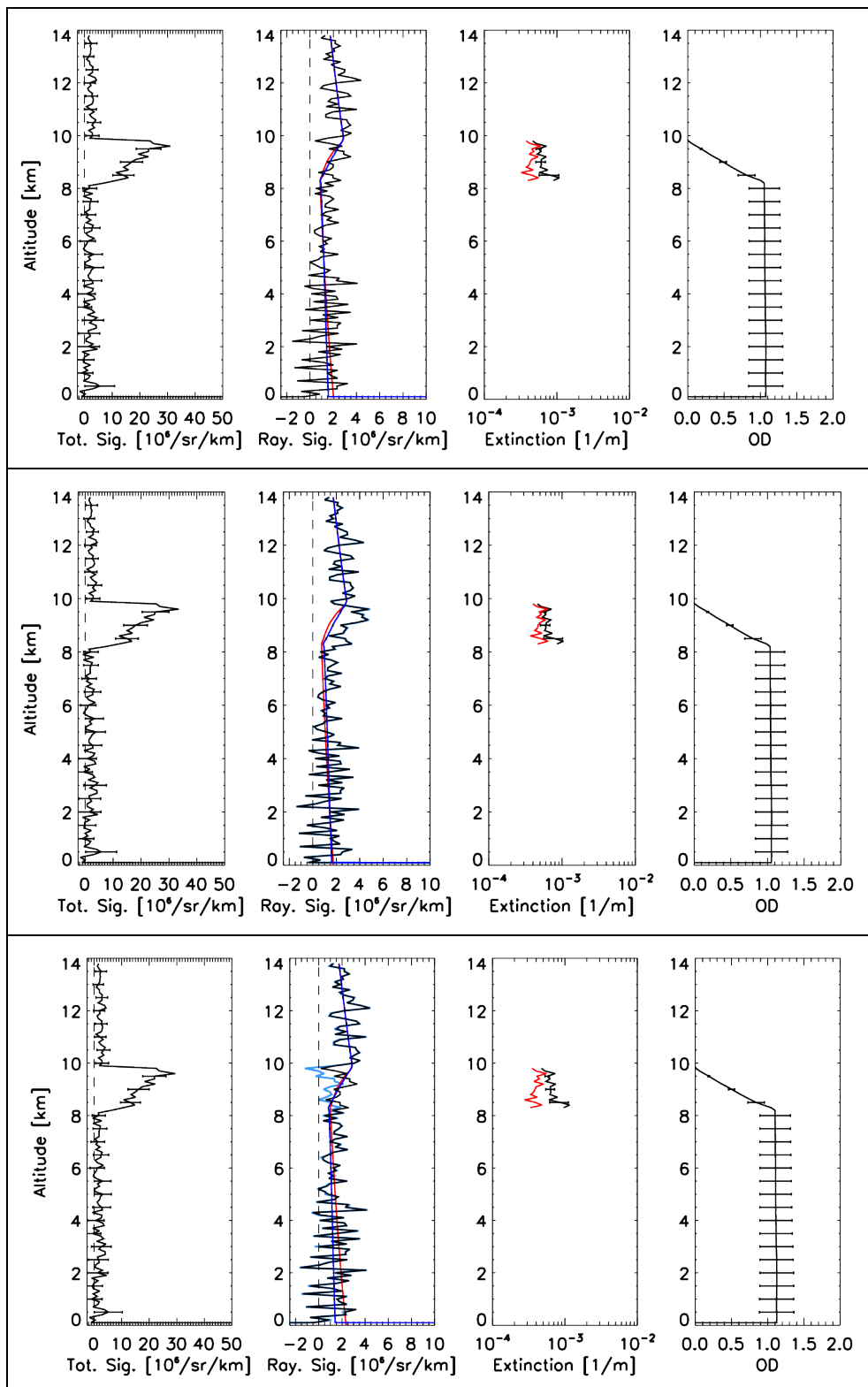


Figure 19: (Top) Same as top of Figure 18 (Middle) same as Case 1a except with at 50% underestimation of C_x (Bottom) 50% overestimation. In the Middle and Bottom panels the light-Blue line shows the First-Guess profile of the Rayleigh Signal.

6.3 2D Examples: The ECSIM “Standard-Scene”.

The prototype code is capable of processing multi-layer cases and has been applied to the ECSIM “Standard-Scene” containing a mixture of both single-layer and multilayer clouds and aerosols. The extinction and extinction-to-backscatter ratio for this scene are shown in Figure 20. The cirrus, aerosol, and stratus areas are clearly separate in terms of their extinction and extinction-to-backscatter ratio values. The corresponding simulated Mie-para, Ray-Para signals along with the FeatureMask (generated by the algorithm described in [A-FM-ATBD]) are shown in Figure 21.

The retrieved extinction and extinction-to-backscatter ratio fields are shown in Figure 22 Figure 23 and the corresponding a priori values for the ice clouds, water clouds and aerosol compared to the “truth” are listed in Table 9.

Region	S true	Ra true	S_a	σ_{S_a}	Ra	σ_{Ra}
Aerosol	30.3	1.4	51.0	2.0	0.1	0.5
Stratus Cloud	21.0	13.0	20.0	0.2	20	0.5
Cirrus-1	15.2	114.7	20	0.5	50	0.5
Cirrus-2	17.0	95.9	20	0.5	50	0.5

Table 9: True values compared to the a priori values used in standard-scene inversion shown here. Cirrus-1 refers to the thinner upper-level cirrus cloud region while Cirrus-2 refers to the lower level extension.

In Figure 22 it can be seen that the estimated extinction is biased low by about 10-20% this is likely due to a too small a priori error estimate for the cirrus Extinction-to-Backscatter ratio. Consistent with expectations, the error estimates for S and the extinction are lowest where the SNR is the highest with an improved precision with respect to the a priori for most of the cloudy regions. However, it can also be seen that the procedure fails to produce useful error estimates for some regions. This is thought not to be related to any short-coming in the basic algorithm but rather is most likely an implementation (which is still in the prototype stage) issue which has not been resolved at the time of this writing.

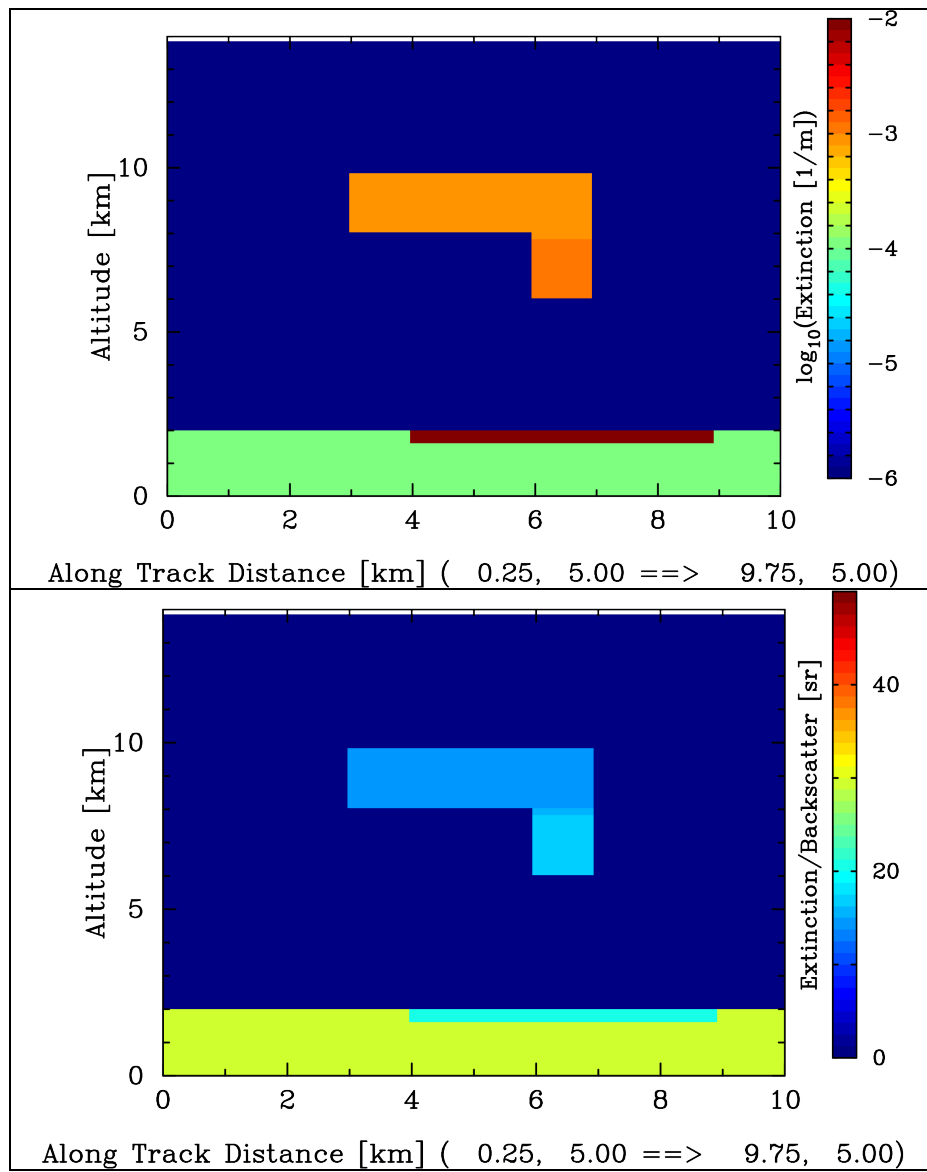


Figure 20: Extinction and S for the “Standard” ECSIM scene.

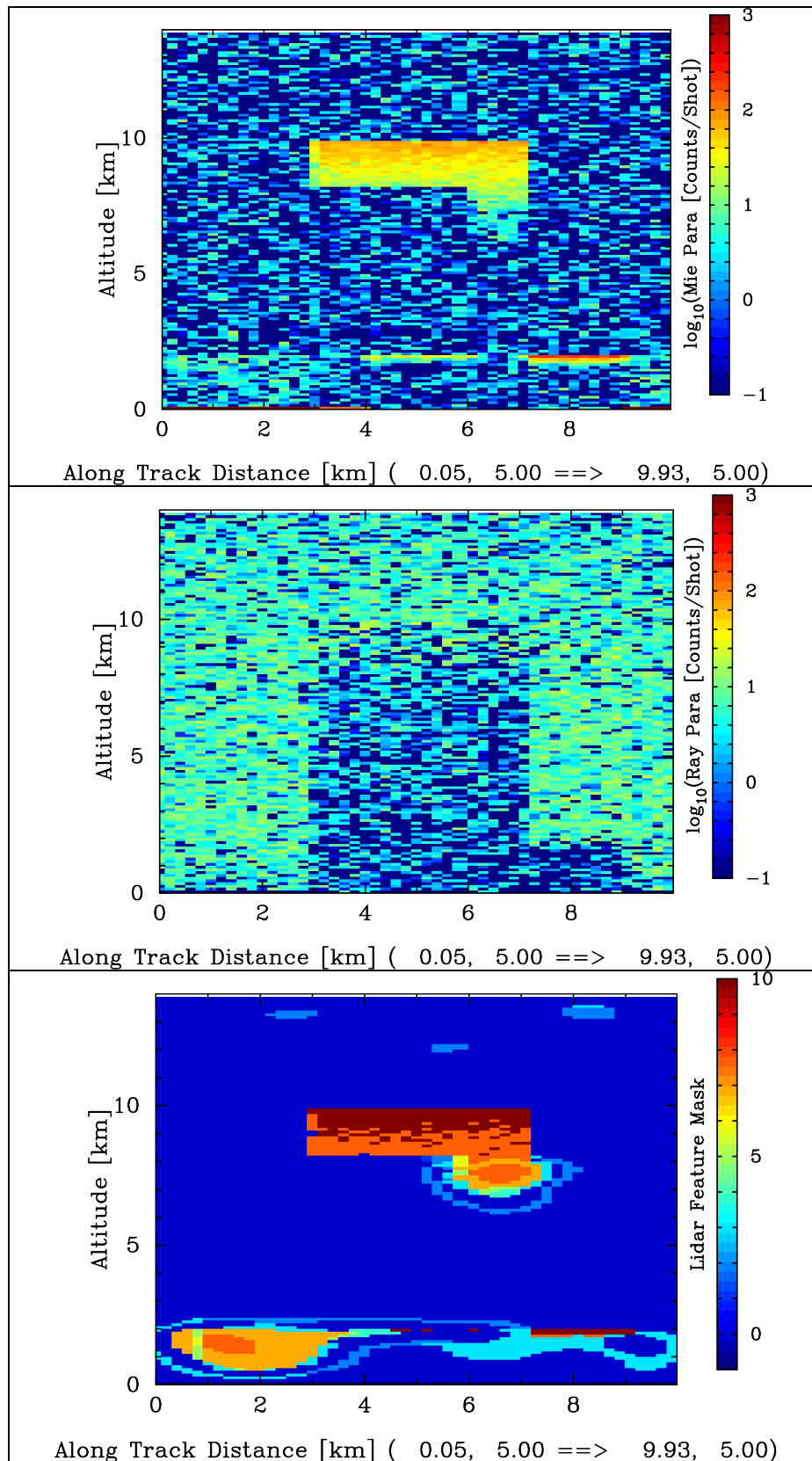


Figure 21: (Top) Cross-talk corrected Mie channel signals corresponding to night-time corresponding to Figure 20 (Middle) Rayleigh channel signals and (Bottom) the corresponding FeatureMask used derived from the Mie channel signals and used as input in this algorithm

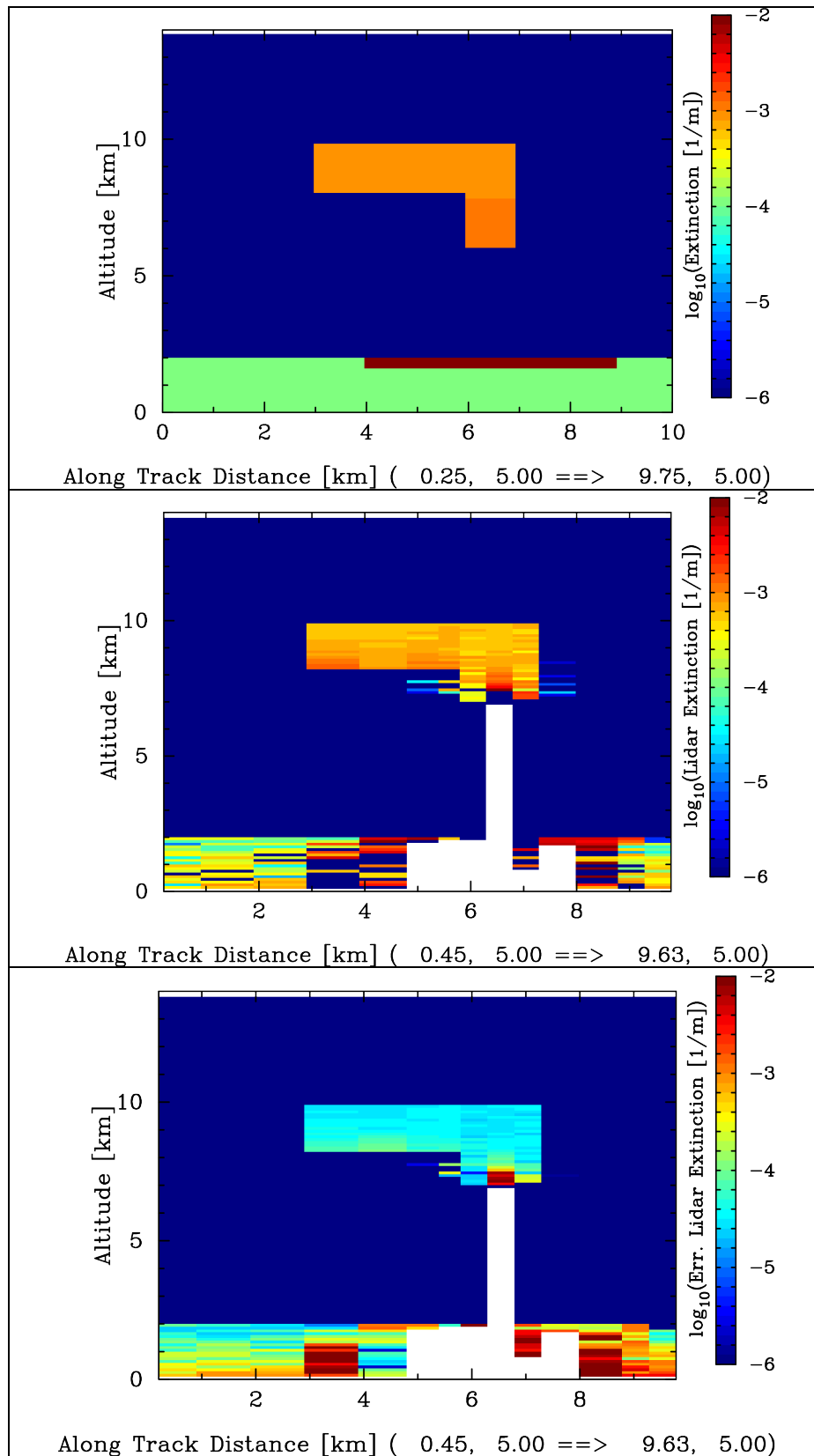


Figure 22: Top : “True” Extinction. Middle: Retrieved best estimate and (Bottom) Estimated error. The blanked regions show areas where clouds or aerosols may be presented but no retrieval is possible due to too low SNR.

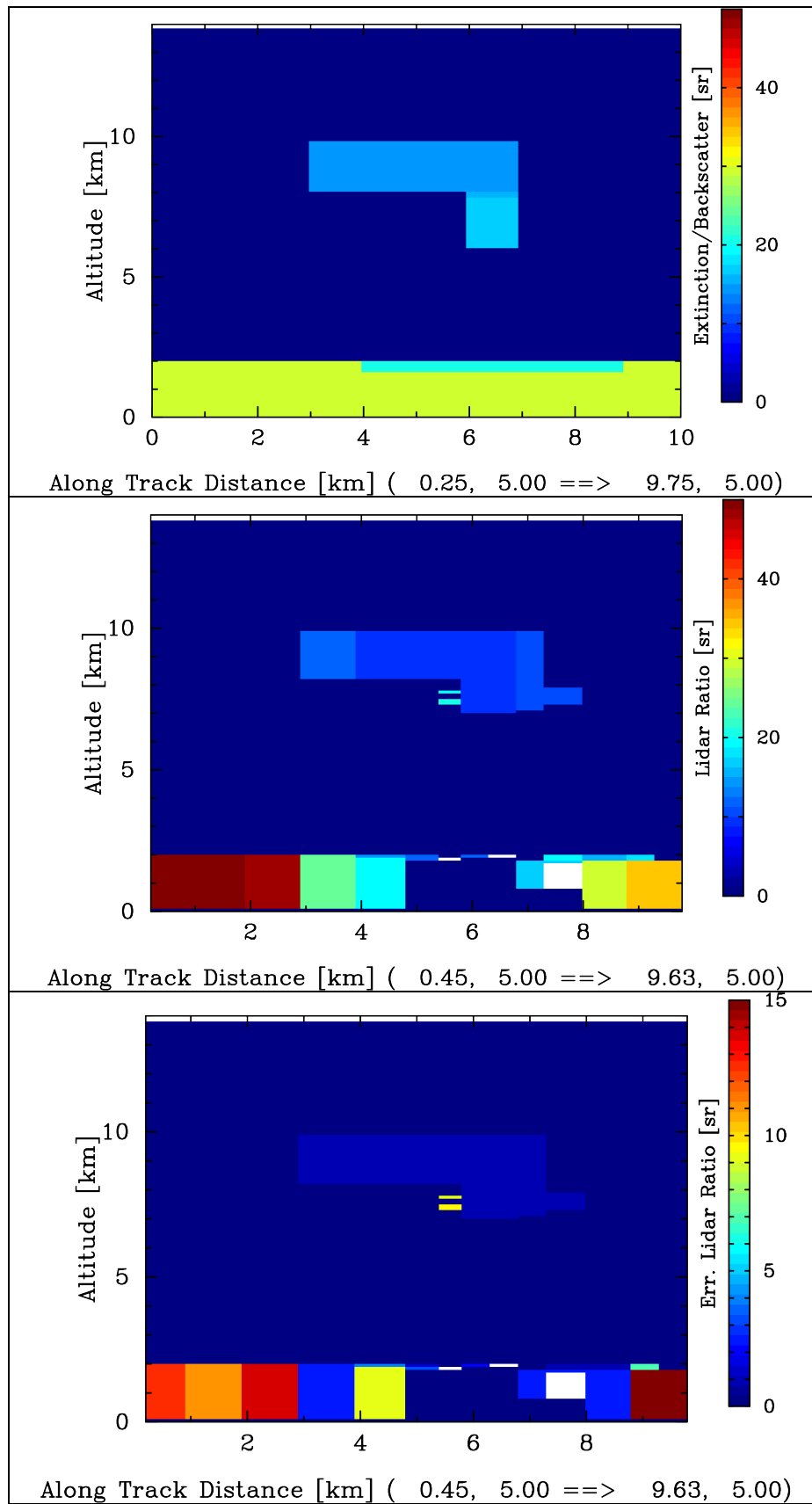


Figure 23: Top: Ideal Extinction-to-Backscatter ratio. Middle retrieval and (Bottom) estimated error.

6.4 2D Examples: ECSIM “Fractal Cirrus Scene”.

The prototype procedure has also been applied to cirrus cases generated by ECSIM aided by the use of the “fractal cloud generator” developed by [Hogan and Kew 2005]. A 3D view of the scene in terms of the extinction field is shown in Figure 24. The scene has an inhomogeneous cloud structure and the Extinction-to-Backscatter ratio varies between about 11 and 17.

The signals and Featuremask corresponding to a satellite overpass through the middle of the scene is shown in Figure 25 and the corresponding extinction and S ratios are shown in Figure 26 and Figure 27 respectively. Here an a priori value for S of 20 was used with an uncertainty of +/50%. Here it can be seen that the optimal extinction retrieval is a marked improvement over the first-guess retrieval with a seemingly good correspondence between the true values and the retrievals in spite of the biased a priori S specification. Also, the extinction error estimates in this case seem appropriate and only reach large values in areas in where the cirrus optical depth is near to fully attenuating the signal. With respect to the S retrievals it can be seen that the retrievals are biased towards the a priori in the thinner parts of the cloud. However, the agreement is better in the thicker parts. Encouragingly, the error estimates associated with the thinner areas are correspondingly larger than for the thicker parts.

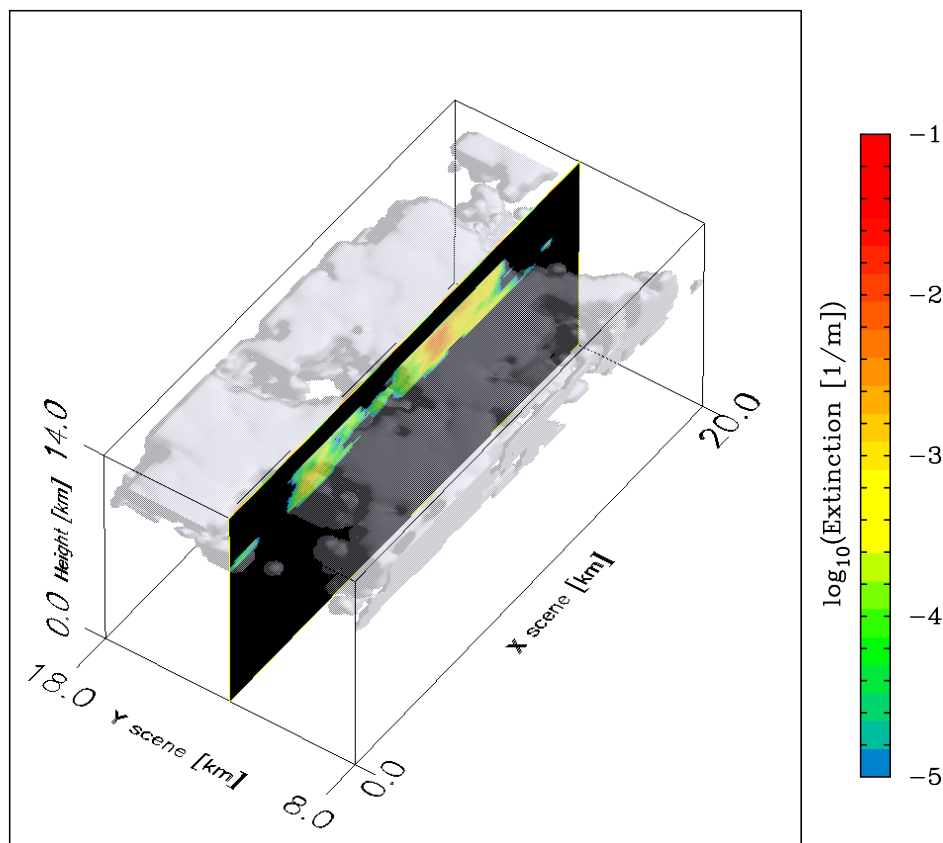


Figure 24: 3D view of the extinction field for the fractal-cirrus scene

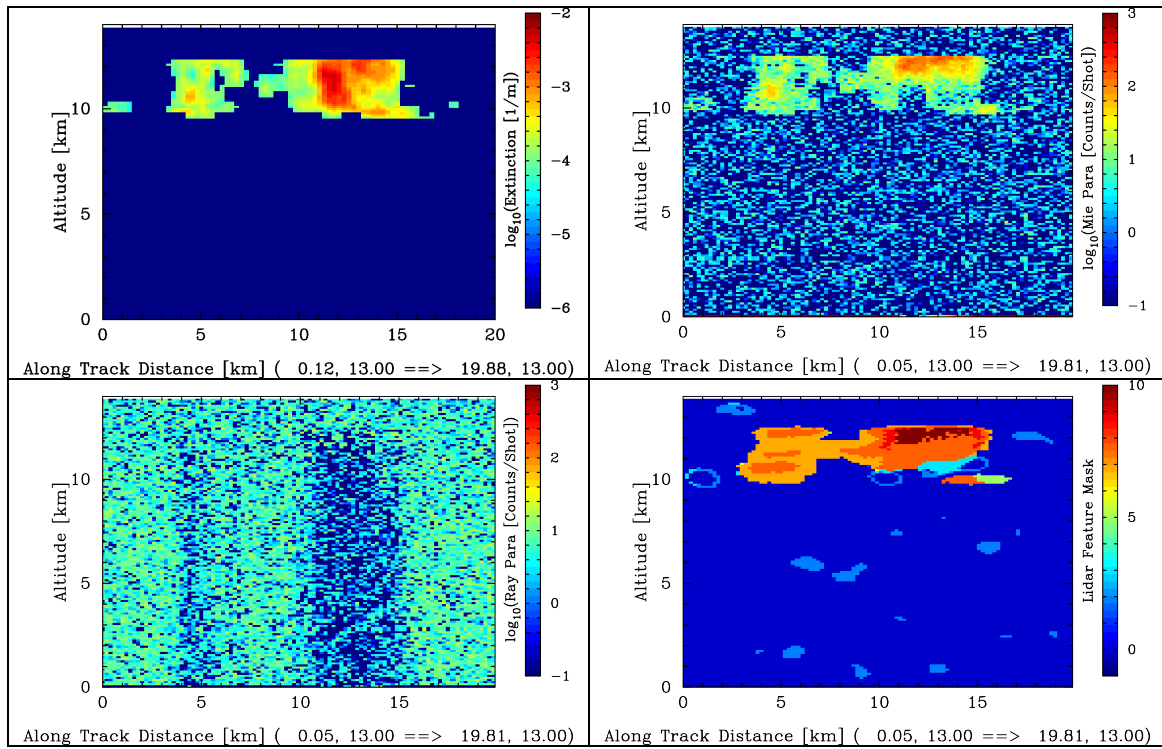


Figure 25: Ideal extinction (Top Left), Mie channel signals (Top right), Rayleigh channel signals (Bottom-Left) and FeatureMask (Bottom-Right) corresponding to the crosssection in Figure 24.

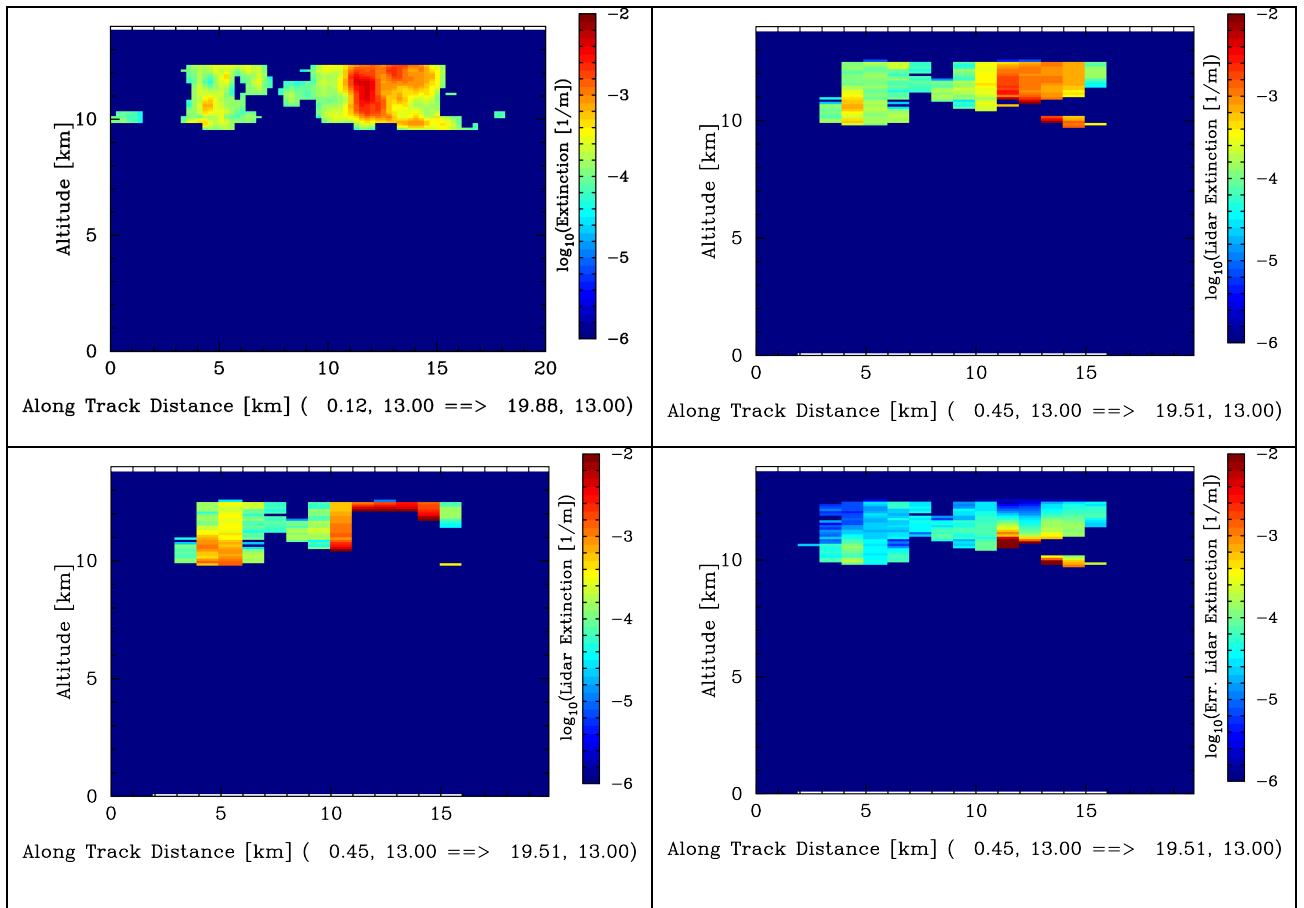


Figure 26: Top-Left : “True” Extinction. Top-Right: Retrieved best estimate. Bottom-Right Estimated error and Bottom-Left: Extinction retrieval produced by the first-guess state-vector.

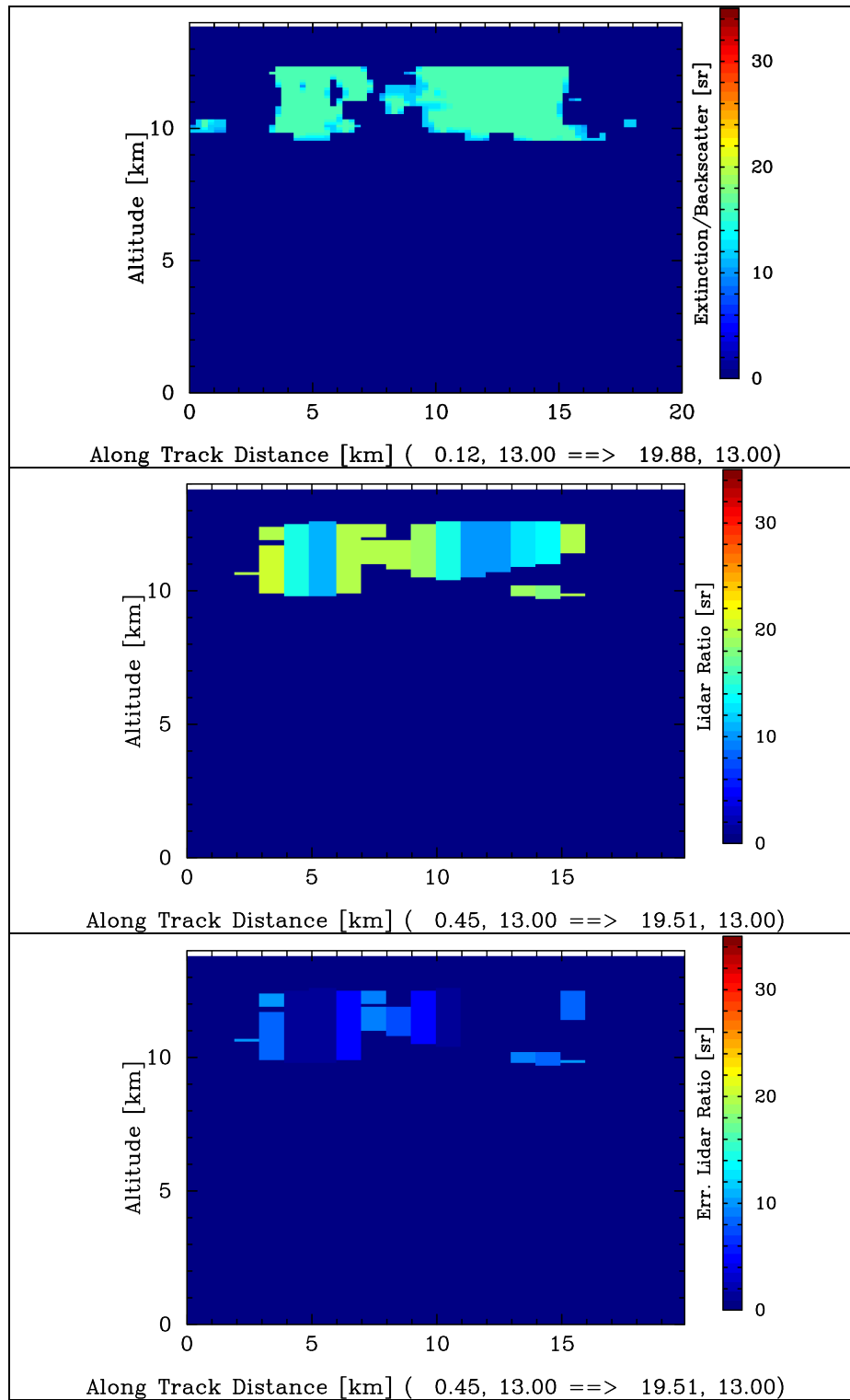


Figure 27: Top: Ideal Extinction-to-Backscatter ratio. Middle retrieval and (Bottom) estimated error.

6.5 SAMUM1Desert Dust Aerosol scene

Up to now the evaluation examples presented have focused on clouds. Here example results for a scene constructed using actual airborne HSRL desert-dust aerosol observations and in situ observations are presented. The extinction field and the simulated Mie and Rayleigh signal profiles averaged to 10 km horizontal resolution are shown in Figure 28. The scene is quantitatively based on the observations made during the SAMUM1 field campaign using the DLR Falcon and is described in more detail in [ICAROHS-TN2]. Here the aerosol has a Backscatter-to-Extinction ratio of about 70.

Sample inversion results using an a-priori value of 70 sr with an uncertainty range from 35-140 sr are shown in Figure 29. Here it can be seen that the results at the 1-km scale are very noisy. Given that the input a priori value (which in practice will be supplied by the large scale Aerosol extinction and backscatter algorithm [A-AER-ATBD]) closely matches the “truth” it is unsurprising that the retrievals values are close to this value. However, the estimated uncertainty in this case is about a factor of 30-50% which is notably less than the a priori factor of 100%.

As may be expected it was found that the retrievals applied at the 1-km scale in this case are very dependent on the a priori S value. 50 km averages of 1-km scale inversion results are shown in Figure 31. Here results for $S_a = 70, 35$ and 140 sr are presented. It can be seen that the average extinction results are indeed sensitive to S_a although a small improvement with respect to the average first guess profiles is obtained. This is in contrast to the case where the inversion is applied to signals which are first averaged to 25 km (Figure 32). In this case a marked improvement over the first guess profile is obtained by the optimal-estimation procedure.

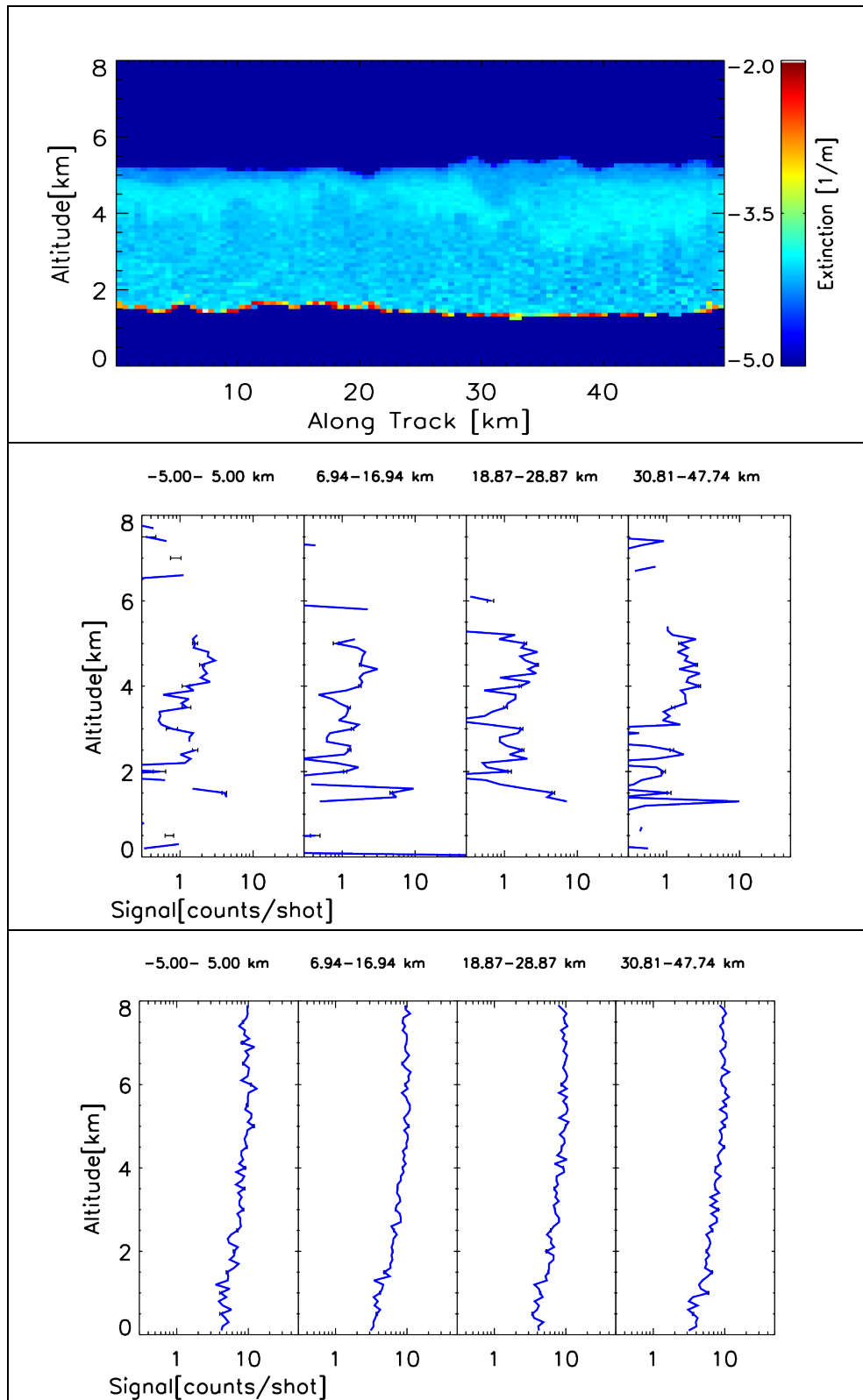


Figure 28: Extinction field and 10km horizontally averaged Mie and Rayleigh signals. The large extinction values below 2 km correspond to the surface.

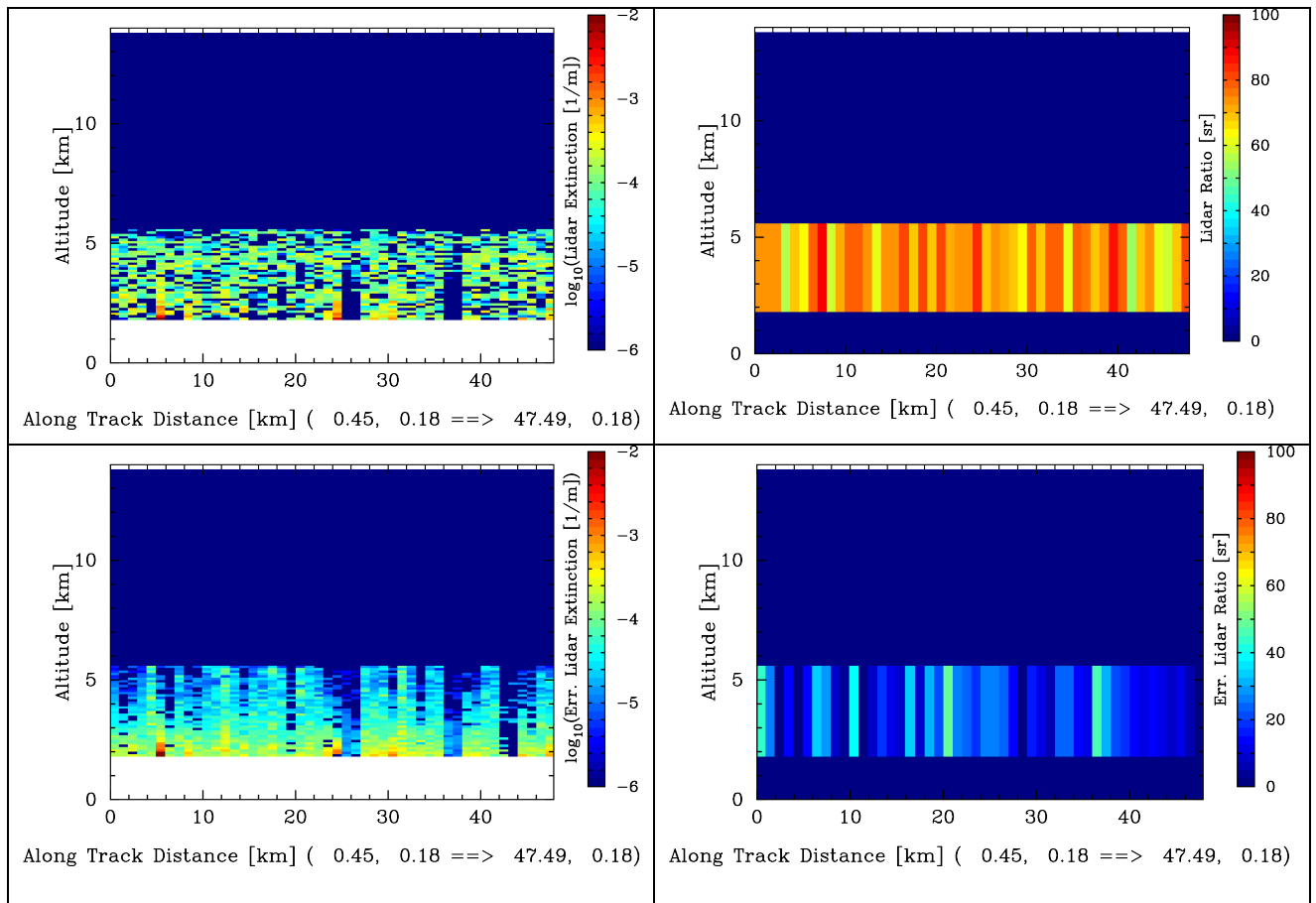


Figure 29: Results of the inversion algorithm applied to 1-km data. Top-Left: Extinction. Bottom-Left: Estimated extinction error. Top-Right: Extinction-to-Backscatter estimated error. Bottom-Right: Estimated error in S .

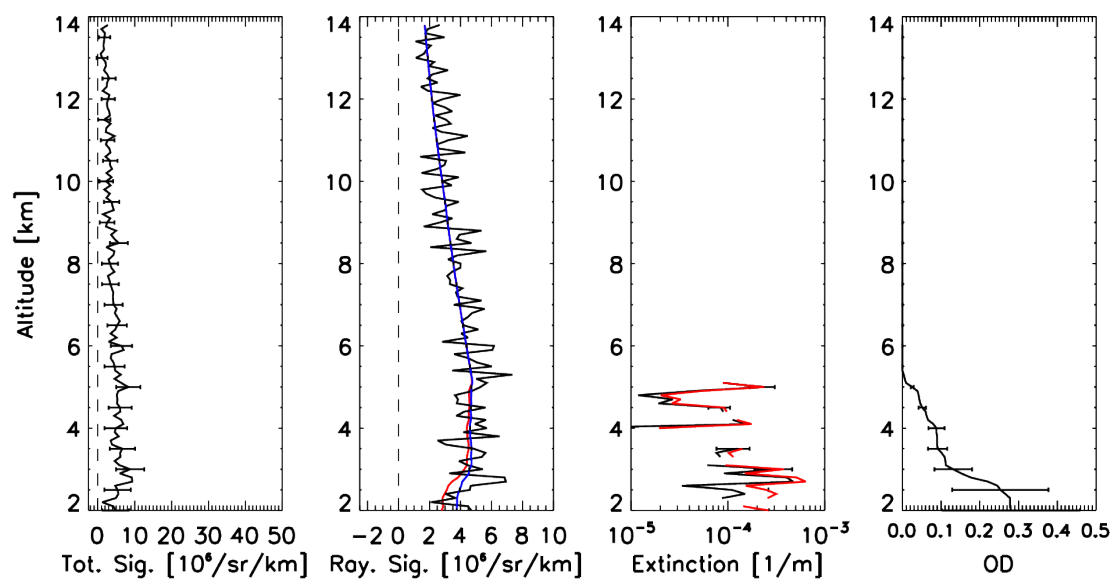


Figure 30: Sample 1km inversion result profiles corresponding to the first retrieval column of Figure 29.

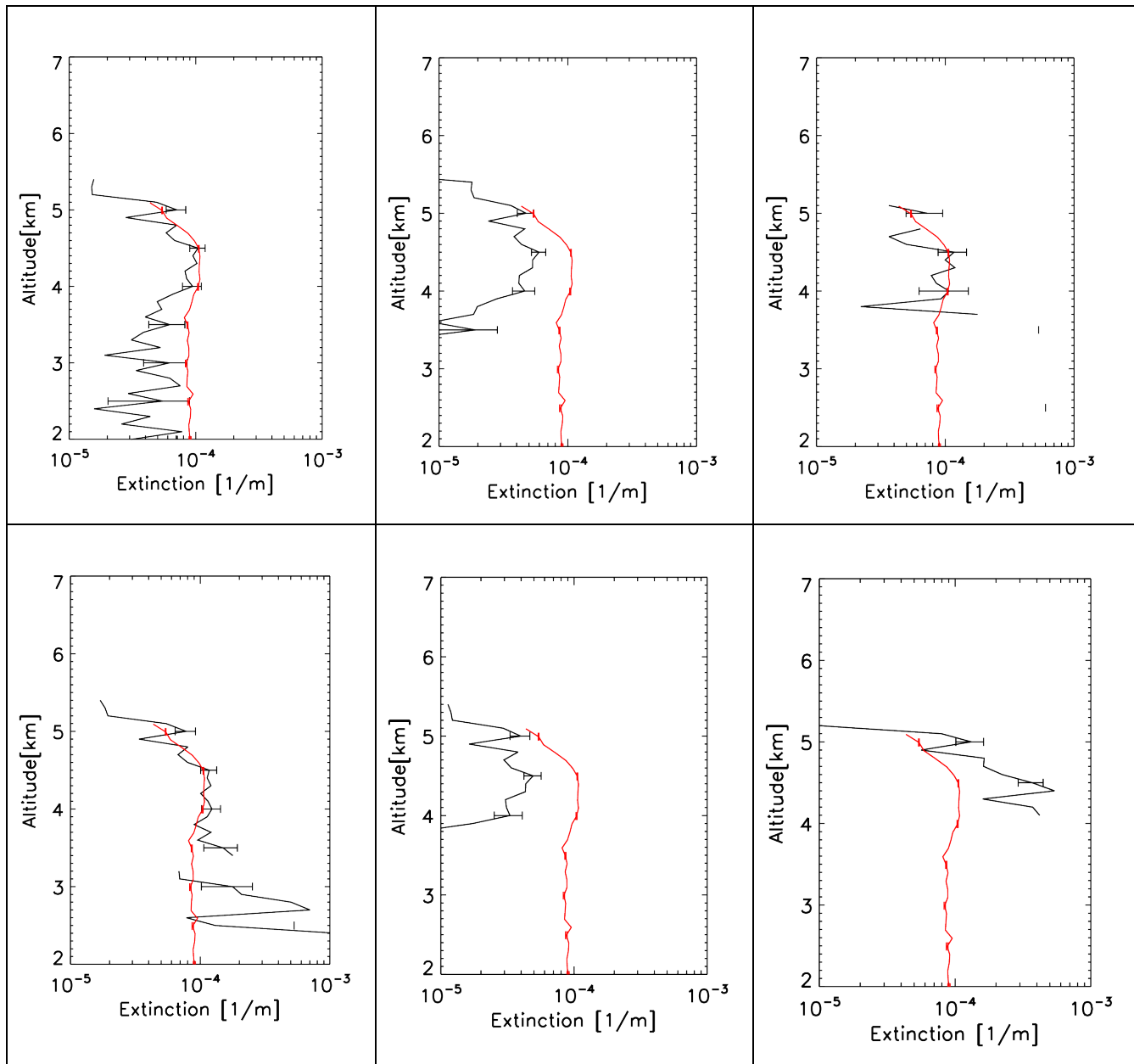


Figure 31: 50km horizontal averages of 1-km inversion results. The Black-lines show the retrieval results while the Red-lines show the true average profile. Left-Column: $S_a = 70$ sr. Middle-Column: $S_a = 35$ sr. Right-Column $S_a = 140$ sr. Top-Row: Average Optimal-Estimate profile. Bottom-Row: Average First-guess profile.

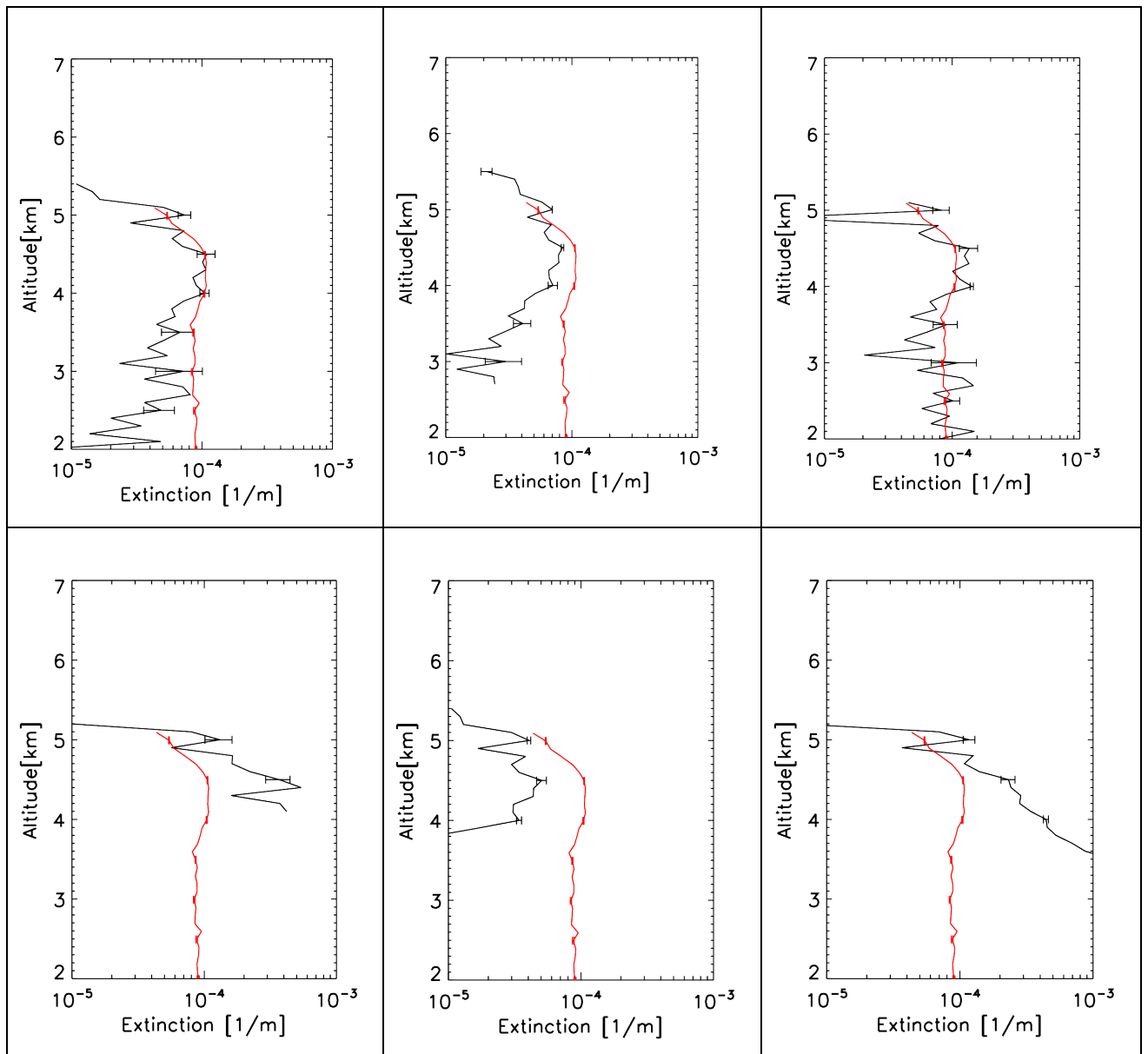


Figure 32: Inversion results applied to 25km averaged signals. The Black-lines show the retrieval results while the Red-lines show the true average profile. Left-Column: $S_a = 70$ sr. Middle-Column: $S_a = 35$ sr. Right-Column $S_a = 140$ sr. Top-Row: Average Optimal-Estimate profile. Bottom-Row: Average First-guess profile.

6.5.1 Sensitivity to Calibration Errors

Example retrievals for this scene assuming that the signal calibration is either 20% too-high or too-low are shown in Figure 33 while a 15% a priori uncertainty was assumed for all calibration and cross-talk coefficients. Here it can be seen that the simulated calibration error leads to very bad first guess retrievals (in the “too-low” case the retrieval profile is even fully negative). However, the optimal estimation extinction profiles are all comparable within their respective errors to the inversion assumed using the “perfect” calibration constants.

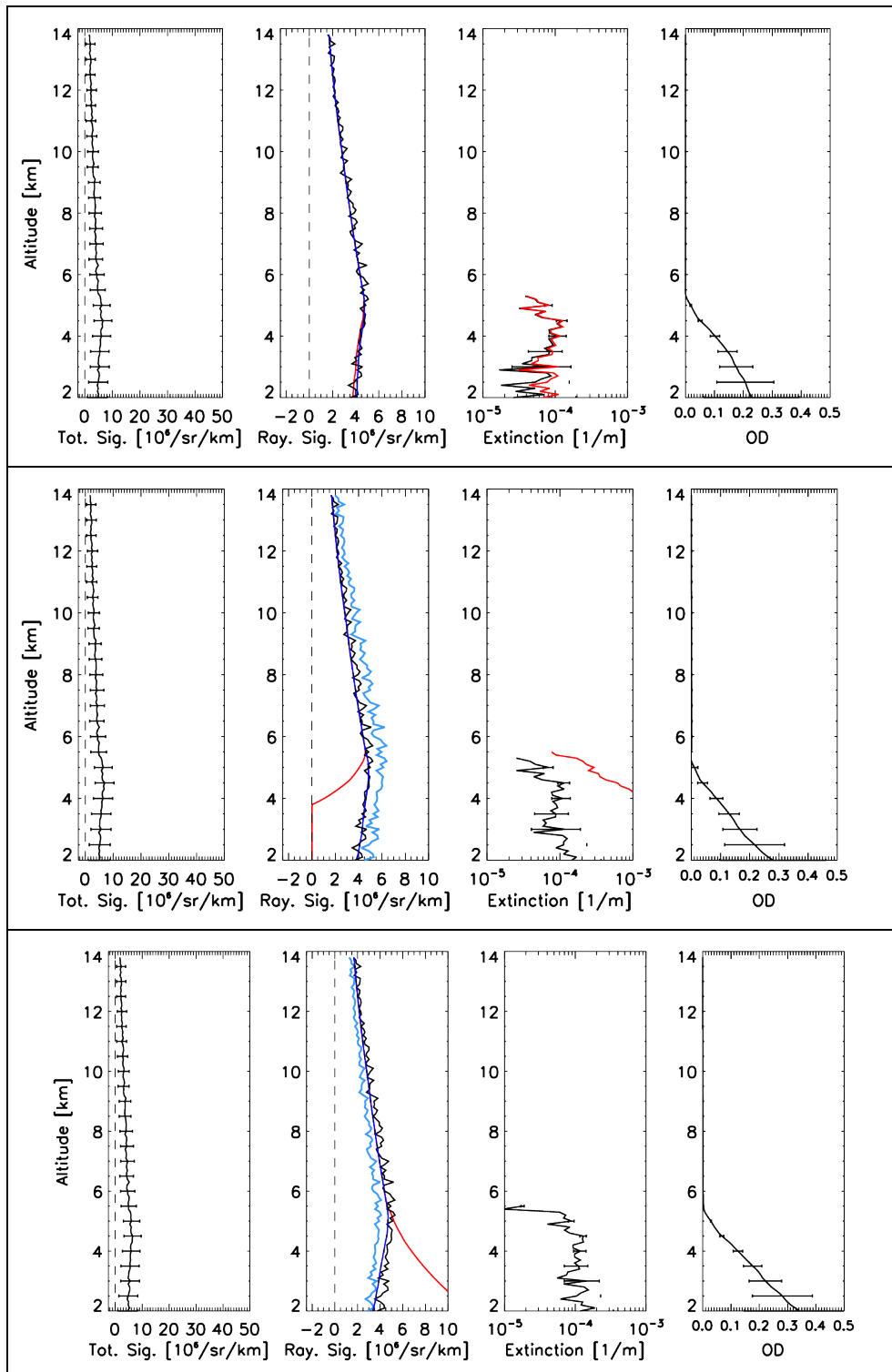


Figure 33: Inversions applied to 25 km averaged signals. (Top) perfect calibration assumed (Middle) calibration coefficients 20% too high (Bottom) calibration coefficients 20% too-low. The Blue line in the middle panes shows the starting value of the Rayleigh backscatter profile while the Red-lines shows the first-guess extinction retrieval.

7 Validation Status

It has been demonstrated that a real improvement in retrieved Extinction and Extinction-to-Backscatter ratios is achieved by using an optimal estimation base approach. This is compared with the case of Klett-based retrievals, and though not discussed in any depth here, much more precise than direct Rayleigh signal derivative based inversions on high resolution horizontal and vertical scales. In short, the goal of wedding the high precision (but low accuracy) of Klett-based approaches with the high accuracy (but low precision) of Rayleigh signal derivative based methods has arguably been convincingly demonstrated.

It goes almost without saying that much validation and development remains before the procedure described in this work reaches maturity. Since there is no available (or foreseen, barring ATLID itself) of space-based lidar signals similar enough to EarthCARE simulations, such as those generated by ECSIM will continue to play a key role in any further development work. In the future the focus will shift towards the use of larger scenes derived from observations (i.e. for example, those built as part of the ICARHOS project [ICAROHS-TN2]) and those built using cloud resolving atmospheric models.

In addition, any practical implementation this algorithm requires the specification of a number of parameters which depend on the desired output resolution and the scale of the cloudy features themselves. In particular, the maximum number of allowed layers and allowed sub-columns must be set. As these parameters will impact the algorithm performance, including data product storage size, it will be desirable to optimize the choices for these two and other parameters. This may be accomplished by suitable analysis of CALIPSO data.

8 Annex A: Technical implementation

The prototype implementation typically can process a 20km ECSIM scene with multilayer-layer clouds present in most of the horizontal domain in 2-3 seconds on a Intel(R) Core(TM)2 Extreme CPU X9100 @ 3.06GHz equipped laptop. This will have to be improved. It should be noted that at the time of this writing that relatively little effort has been directed to improving the speed of the algorithm. It is likely that code improvements and optimizations, including the replacement of numerical derivative calculations by analytical calculations, together with the use of more capable hardware could dramatically reduce the execution time.

8.1 External models

- The GPL licensed multiple scattering code of R. Hogan (Hogan 2006) is an important component of this algorithm see <http://www.met.reading.ac.uk/clouds/multiscatter/>
- A public domain implementation of the BGSF minimization routine using numerical derivatives has been used. The code was downloaded from <http://athens.src.uchicago.edu/jenni/econ350/Salvador/MINIMIZATION.F90> and subsequently modified by allowing for variable fixed allowed maximum step sizes.

The choice of minimization routine is not central to the algorithm however, and other suitable minimization solvers can be used. The present version is an adaptation of the method described in Press et al. (1992) modified so that numerical derivatives are used.

- A public domain implementation of a square-matrix inversion routine has also been used. As with the minimization solver, the choice of inversion routine is not central to the algorithm however and other suitable matrix inversion solvers can be used.
-